# Deep Learning Improves Global Satellite Observations of Ocean Eddy Dynamics

**Scott A. Martin[1], Georgy E. Manucharyan[1], and Patrice Klein[2,3]**

[1]School of Oceanography, University of Washington, Seattle, WA, USA
[2]Jet Propulsion Laboratory, California Institute of Technology, Pasadena, CA, USA
[3]Laboratoire de Météorologie Dynamique, École Normale Supérieure, Paris, France

**Key Points:**

- We develop the first deep learning global estimates of surface ocean currents from multi-modal satellite observations.
- Our deep learning method is able to map surface currents with state-of-the-art resolution and accuracy.
- The diagnosed kinetic energy cascade is an order of magnitude higher compared to conventional altimetry products.

Corresponding author: Scott A. Martin, smart1n@uw.edu

## Abstract

Ocean eddies affect large-scale circulation and induce a kinetic energy cascade through their non-linear interactions. However, since global observations of eddy dynamics come from satellite altimetry maps that smooth eddies and distort their geometry, the strength of this cascade is underestimated. Here, we use deep learning to improve observational estimates of global surface geostrophic currents and explore the implications for the cascade. By synthesizing multi-modal satellite observations of sea surface height (SSH) and temperature, we achieve up to a 30% improvement in spatial resolution over the community-standard SSH product. This reveals numerous strongly interacting eddies that were previously obscured by smoothing. In many regions, these newly-resolved eddies lead to nearly an order-of-magnitude increase in the upscale kinetic energy cascade that peaks in spring and is strong enough to drive the seasonality of large mesoscale eddies. Our study suggests that deep learning can be a powerful paradigm for satellite oceanography.



## Plain Language Summary

We developed a deep learning method to estimate global maps of surface ocean currents from satellite observations with significantly improved resolution and accuracy compared to existing methods. These maps dramatically improve our ability to observe eddy dynamics and the impact of eddies on the transfer of energy between scales in the ocean. Our study suggests that deep learning can be a powerful paradigm for satellite oceanography.


## 1 Introduction

Mesoscale eddies (50-300 km) are a critical component of the global ocean circulation, transporting dynamical and biogeochemical tracers (Wunsch, 1999; Jayne & Marotzke, 2002; Zhang et al., 2014). Despite being the ocean's dominant reservoir of kinetic energy (KE), the sources and sinks of mesoscale eddy KE remain poorly constrained (Ferrari & Wunsch, 2009). One major process affecting mesoscale KE is the transfer of KE between scales by non-linear eddy interactions, known as the KE cascade (Scott & Wang, 2005; Aluie et al., 2018; Klein et al., 2019). There is growing evidence that non-linear eddy interactions induce a strongly seasonal upscale KE cascade, KE transfer from small to large scales, that is intensified in winter and spring (Sasaki et al., 2014; Qiu et al., 2014; Uchida et al., 2017; Schubert et al., 2020; Ajayi et al., 2021; Balwada et al., 2022; Naveira Garabato et al., 2022; Steinberg et al., 2022; Lawrence & Callies, 2022; Schubert et al., 2023; Storer et al., 2023). The strength of non-linear eddy interactions and the KE cascade are set by the vorticity and strain of eddies (Aluie et al., 2018; Klein et al., 2019), which are highly sensitive to the geometry of eddies. There is thus a need for global observations of eddies with sufficient resolution to accurately diagnose vorticity and strain - this motivates our study.

Satellite observations of the surface expressions of eddies are a powerful observing system for eddy dynamics since satellites resolve a wide range of scales compared to in situ observations (Klein et al., 2019), however, there are challenges in inferring surface currents from satellite observables. Satellite altimetry allows the estimation of eddies by mapping their expression in sea surface height (SSH), which is used to estimate surface geostrophic currents (Chelton et al., 2001). Conventional altimeters measure SSH and resolve mesoscale eddies along each satellite's track (Dufau et al., 2016) but leave large gaps between tracks that must be interpolated to diagnose eddy dynamics. Meanwhile, satellites observe high-resolution 2D snapshots of sea surface temperature (SST) but there are gaps due to clouds and the relationship between SST and surface currents is complex (Isern-Fontanet et al., 2006, 2014; Rio et al., 2016).

Conventionally, surface currents are estimated either via data assimilation (DA) (Lellouche et al., 2021; Le Guillou et al., 2021, 2023) or objective analysis (OA) of SSH (Taburet et al., 2019; Ubelmann et al., 2015, 2021, 2022). DA provides 3D state estimates approximately consistent with the physics of a numerical model, typically a general circulation model (GCM). However, state-of-the-art DA systems (Lellouche et al., 2021) use GCM resolutions that only partially resolve mesoscale dynamics and so suffer high errors in SSH and surface currents at mesoscales due to unresolved eddy dynamics and the lack of high-resolution 3D in-situ observations. In contrast, OA allows to estimate only the 2D SSH field using a statistical approach (Taburet et al., 2019; Ubelmann et al., 2015, 2021, 2022), from which currents can be estimated through geostrophy and further empirical corrections for winds (Rio et al., 2014), equatorial dynamics (Lagerloef et al., 1999), and cyclo-geostrophy (Penven et al., 2014; Cao et al., 2023), or potentially using machine learning (Sinha & Abernathey, 2021; Xiao et al., 2023). Surface currents derived from OA SSH fields give eddy amplitudes and configurations more consistent with observations than DA since they are not biased by unresolved dynamics. However, OA is a fundamentally statistical approach that does not guarantee a physically consistent reconstruction and biases in the covariance models used in OA could bias the reconstructions. OA artificially suppresses variance at smaller scales, smoothing and distorting eddies (Ballarotta et al., 2019). This leads to a significant underestimation of crucial dynamical quantities, like vorticity and strain.

Deep learning has recently emerged as an alternative approach for estimating surface currents. A number of proof-of-concept studies demonstrate that neural networks can be trained to map SSH or surface currents from altimeter observations through either 'simulation learning' using synthetic data from high-resolution GCMs (Fablet et al., 2021; Manucharyan et al., 2021; Buongiorno Nardelli et al., 2022; Beauchamp et al., 2022; Fablet et al., 2023; Thiria et al., 2023; Febvre et al., 2024; Archambault et al., 2024; Kugusheva et al., 2024) or 'observation-only learning' from real-world satellites (Martin et al., 2023; Archambault et al., 2023). Deep learning allows the optimal mapping to emerge objectively from the data by removing OA's need to prescribe linear covariance models (Taburet et al., 2019), and also allows the use of SST observations as an additional input to improve the mapping between altimeter observations (Buongiorno Nardelli et al., 2022; Fablet et al., 2023; Martin et al., 2023; Archambault et al., 2023, 2024). Simulation learning showed promising results on synthetic observations in proof-of-concept studies. However, transferring these methods to real-world observations remains a challenge since GCMs are not exact analogs of the real world and neural networks behave unpredictably when applied to data different from that used during training. This domain gap can be partly addressed through fine-tuning on real-world observations (Febvre et al., 2024; Archambault et al., 2024). More fundamentally, simulation learning blurs the boundary between observations and GCMs, much like DA. In contrast to simulation learning, observation-only learning, analogous to OA, is directly applicable to real-world observations and is uncontaminated with GCM biases. This comes at the expense of smoothing some smaller-scale features due to the limited resolution of real-world observations. Nonetheless, regional proof-of-concept studies have shown observation-only learning can give SSH maps with significantly higher resolution than OA, leading to significant improvements in the estimation of vorticity and strain (Martin et al., 2023; Archambault et al., 2023).

Extending regional proof-of-concept studies to global SSH mapping poses a significant challenge for deep learning because the global ocean exhibits spatiotemporally diverse dynamics. Given the sparsity of the altimetry record for observation-only learning, it remains to be demonstrated that a neural network can generalize across all dynamical regimes. We hypothesize that observation-only learning can be used to create global SSH maps with enhanced resolution, and that this will radically improve global observations of vorticity and strain - and hence of non-linear eddy dynamics. Here, we develop the first global deep learning estimates of surface currents. We evaluate their

accuracy, their ability to resolve vorticity and strain, and explore the resulting KE cascade. By disseminating our new global SSH product, we hope to enable more accurate studies of eddy dynamics and their impact on general ocean circulation, marine ecosystems, and climate.

## 2 Methods

### 2.1 NeurOST: Global SSH Maps from Altimetry and SST Using Deep Learning

We train a neural network to map SSH from sparse altimeter observations (E.U. Copernicus Marine Service Information (CMEMS), 2024b, 2024a) and gridded SST (JPL MUR MEaSUREs Project, 2015). Our approach, illustrated in Figure 1, builds upon that described in our recent proof-of-concept study (Martin et al., 2023) and is described in full in S.I. S1.1-5.

We use 'self-supervised' learning, taking a time series of altimeter observations within a local subdomain (30 days by 960 km by 960 km) from all but one of the available altimeters alongside the corresponding SST as input to a neural network tasked with reconstructing 2D SSH. The objective minimized during training is the mean square error of the mapped SSH calculated against the withheld altimeter. We restrict the mapping to local subdomains since eddy dynamics are local, so a global 'field of view' is likely unnecessary to reconstruct eddies in any local subdomain.

We use kernel-weighted averaging to combine thousands of overlapping subdomain SSH maps together into a single global SSH map (S.I. S1.5 and Callaham et al. (2019)). Using a large set of subdomain examples drawn from across the globe, we train a single network to map SSH in all regions, achieving generalization across diverse regional dynamics. By training a single global network rather than an ensemble of bespoke regional networks we avoid arbitrarily dividing the globe into regions and learn a general and robust SSH mapping. The network was trained on observations from 2010 to 2023, with 2019 withheld for validation (Figure S8).

We refer to our method as 'NeurOST (SSH-SST)' (Neural Ocean Surface Topography). To assess the value of SST we also trained a network to map SSH from altimetry alone; 'NeurOST (SSH)'.

### 2.2 Estimating Surface Currents from SSH

Large-scale ocean currents satisfy geostrophic balance, allowing surface currents to be estimated from SSH through geostrophy (S.I. Equation 1). The limitations of geostrophy and potential empirical ageostrophic corrections (Lagerloef et al., 1999; Rio et al., 2014; Penven et al., 2014; Cao et al., 2023) are discussed in S.I. S1.1 where we also show diagnostics of eddy dynamics (e.g. KE cascade) are only weakly sensitive to the correction for cyclo-geostrophy of Penven et al. (2014). Thus, throughout this manuscript, the presented surface currents were calculated using geostrophy.

### 2.3 SSH Mapping Evaluation: Observing System Experiment (OSE)

We employ an observing system experiment (OSE) to evaluate the SSH maps. Comparisons to existing methods are achieved using an Ocean Data Challenge (Metref et al., 2023; Metref & Ballarotta, 2023) in which developers of different methods implement them on a common experiment. In the OSE used here, we create global SSH maps for 2019 using all altimeters apart from Saral/Altika that is used to evaluate the maps. Accuracy is evaluated using root mean square error (RMSE), and we quantify the maps' effective spatial resolution following Ballarotta et al. (2019) to estimate the smallest resolved wave-

length. We compare NeurOST to the community-standard 'DUACS' product (Le Traon et al., 1998; Taburet et al., 2019) as well as to the 'MIOST' method (Ubelmann et al., 2021; Ballarotta et al., 2023). Surface geostrophic currents are evaluated using drifters (E.U. Copernicus Marine Service Information (CMEMS), 2024c). Additionally, we compare NeurOST to proof-of-concept methods in the Gulf Stream Extension using a similar Ocean Data Challenge that was regional in scope (Ballarotta et al., 2021). More details are in S.I. S1.6-7.

### 2.4 Eddy Dynamics Evaluation: Observing System Simulation Experiment (OSSE)

While the OSE evaluates SSH maps, we cannot use it to evaluate eddy dynamics (vorticity and strain) inferred from SSH as this requires access to the full 2D eddy field. We therefore conduct an observing system simulation experiment (OSSE) where we generate synthetic altimeter observations from the 1/12° GLORYS reanalysis (Lellouche et al., 2021; E.U. Copernicus Marine Service Information (CMEMS), 2024d) and use them in combination with GLORYS SST as input to NeurOST with no additional training on GLORYS. We then compare the resulting NeurOST maps to the 2D ground-truth from GLORYS to evaluate eddy dynamics diagnostics, specifically surface geostrophic currents and vorticity for which we define normalized skill scores representing the fraction of variance explained (S.I. S1.11). This point-wise comparison to GLORYS cannot be made for DUACS since this method is not open source, preventing its implementation on simulated observations.

### 2.5 Kinetic Energy Cascade Diagnosis

We use NeurOST surface geostrophic currents to diagnose the strength of the KE cascade in a range of regions through coarse-graining (Aluie et al., 2018; Storer et al., 2022; Storer & Aluie, 2023; Storer et al., 2023). The strength of the KE cascade is given by the spectral KE flux, which quantifies KE transfer from larger to smaller scales at each wavelength. A positive flux indicates a downscale (forward) cascade, whereas a negative value indicates an upscale (inverse) cascade. More details are in S.I. S1.12.

## 3 Results

### 3.1 State-of-the-Art Global SSH Maps Using Deep Learning

Our new global SSH maps (NeurOST SSH-SST) show rich dynamical structures associated with western boundary currents, abundant mesoscale eddies in the extratropics, and large-scale equatorial waves in the tropics (Figure 1).

The effective resolution of our maps is improved compared to DUACS throughout the global ocean, with a pronounced improvement in western boundary currents and the subtropics where we resolve wavelengths 30% smaller (Figure 2b,d and Table S1). The global RMSE of the mapped SSH is 6% lower than DUACS, while reductions in the RMSE of small mesoscale signals (70-250km wavelengths) reach 20% in regions of intense eddy activity (Figure 2a,c,e and Table S1). Similarly, NeurOST outperforms MIOST in almost all regions, especially for small mesoscale signals, making our method state-of-the-art in global SSH mapping (Figure S1 and Table S1).

Using SST improves the mapping of SSH throughout the global ocean (Figure 2f and Table S1). To assess the utility of SST, we compare the performance of NeurOST with and without SST. The mapping of small mesoscales is improved using SST, especially in the extratropics where mesoscale SSH and SST are correlated (Cornillon et al., 2019) (Figure 2f and Table S1). SST is especially impactful when few altimeters are available (Table S3). While observations from six altimeters were used to create the maps

compared above, for much of the altimetry era there were only two altimeters operational, causing eddies in DUACS to be severely smoothed. We evaluated our network using only two altimeters as input and found that in most regions NeurOST SSH-SST with just two altimeters yields higher-resolution SSH than DUACS achieves with six (Table S3). This highlights the power of using deep learning and SST to extract maximum value from the now thirty-year altimetry record.

NeurOST maps SSH across all regions, unlike prior studies that trained bespoke region-specific networks. While regional networks (Martin et al., 2023; Febvre et al., 2024) in the Gulf Stream offer marginally improved SSH mapping compared to our global network (Ballarotta et al., 2021) (Table S2), fine-tuning on a smaller set of observations from the Gulf Stream Extension (S.I. S1.6) brings NeurOST in line with state-of-the-art regional networks (Table S2). This shows the potential for further refinement of NeurOST by end users interested only in a single region.

Surface geostrophic currents from our maps are more accurate when evaluated with drifter observations. NeurOST reduces the RMSE of surface currents significantly across the global ocean, especially in the subtropics, where RMSE is reduced by 20% compared to DUACS (Figure S2). Discrepancies between the mapped currents and drifter observations are due to both the accuracy of the mapped geostrophic current and the degree to which real-world currents are in geostrophic balance. Nonetheless, this large reduction in RMSE demonstrates the significant improvement in the mapped currents.

### 3.2 Improved Physical Realism of Mesoscale Eddies

Calculating vorticity and strain from the surface current maps appears to show a significant qualitative improvement in the realism of eddy dynamics in NeurOST (Figure 3b,c,d and Movie S1). NeurOST vorticity shows an abundance of small mesoscale eddies with clearly defined boundaries, many of which are completely absent in DUACS (Figure 3b,c). A contrasting view of eddy dynamics emerges when comparing the temporal eddy evolution: eddies appear to uniformly propagate westward in DUACS, while NeurOST eddies exhibit strong non-linear eddy interactions that deform each other's vorticity cores, causing filamentation (Supplementary Movie S1). These better-resolved nonlinear eddy interactions also manifest in the higher strain rate between eddies seen in NeurOST, evidenced by regions of highly positive Okubo-Weiss quantity (Figure 3d, S.I. S1.10). This increased strain has important implications for eddy dynamics since it is associated with enhanced frontogenesis (Hoskins, 1982; Siegelman et al., 2020) and a stronger KE cascade (Aluie et al., 2018). While vorticity and strain appear qualitatively more realistic in NeurOST than in DUACS, their accuracy cannot be quantified using along-track SSH observations. To demonstrate that NeurOST does not introduce artificial eddies, we test its ability to reconstruct vorticity using synthetic observations from a GCM with our OSSE framework (Section 2.4).

NeurOST, trained on real-world observations and applied now to synthetic observations from GLORYS, skillfully reconstructs surface currents, especially in the subtropics and western boundary currents, where it explains over 70% of the variance (Figure 4a). Its skill deteriorates somewhat in regions of low variability, at high latitudes, and near coasts, where the observational training data is likely to significantly differ from the GLORYS simulation. Since vorticity is highly sensitive to small-scale SSH features, its overall reconstruction skill is slightly lower than that for surface currents. Nonetheless, NeurOST reconstructs a remarkable 50-80% of vorticity variance throughout the subtropics and western boundary currents. Comparing spatial patterns of vorticity and strain, it is clear that NeurOST misses smaller-scale filaments but skillfully reconstructs larger eddies and some larger filaments and is not prone to creating artificial eddies (Fig 4c-f and Supplementary Movie S2). NeurOST reconstructs features as small as 50 km in some cases (see filaments in Figure 4c-f). Thus, NeurOST can reasonably well reconstruct

the 2D vorticity and strain fields despite being trained only on real-world along-track SSH observations and never using real or simulated vorticity/strain fields during training.

Since GLORYS contains finer-scale vorticity features than NeurOST, it can be used to estimate the kinetic energy cascade (see Storer et al. (2023) and Figure S7). However, there is a qualitative difference in eddy dynamics between GLORYS and NeurOST that clearly manifests in small-scale vorticity features. In GLORYS, vorticity features are overwhelmingly dominated by persistent filaments, whereas in NeurOST there is an abundance of smaller-scale coherent eddies with less prominent filaments (Supplementary Movie S1). This difference could be due to the relatively coarse grid of GLORYS (1/12°) that does not resolve the generation of small-scale eddies by submesoscale instabilities in the mixed layer, which are known to be prominent in winter. In such coarse-resolution models, large eddies stir vorticity to form small-scale filaments, but they can artificially persist and grow, being constrained only by numerical or specified model diffusion. In reality, the presence of small-scale eddies can disrupt this filamentation by large-scale eddies, and filaments often become unstable and form submesoscale eddies (e.g., Taylor and Thompson (2023)). Since there are no ground-truth observations of vorticity, one cannot definitively establish whether there is excessive filamentation in GLORYS or whether NeurOST introduces artificial eddies at small scales. However, looking at the NeurOST reconstruction of GLORYS (Section 2.4), NeurOST appears to provide a coarse-grained view of GLORYS, showing no evidence of artificial small-scale eddies being introduced (compare Supplementary Movies S1 & S2). Furthermore, when reconstructing real-world SSH and surface currents, NeurOST also has significantly lower errors than GLORYS (Figure S3 and Table S1). With increased confidence that NeurOST provides a better estimation of real-world ocean eddy dynamics, we now proceed to explore its impact on our understanding of the KE cascade and seasonality of mesoscale eddies.

### 3.3 Seasonal Kinetic Energy Cascade

A distinct seasonality in eddy dynamics emerges in our maps that was largely absent in DUACS, with smaller scale eddies peaking in intensity in the winter and spring. The mesoscale KE and strain rate throughout the subtropics are 50-100% higher in NeurOST than in DUACS in winter/spring, whereas they are comparable in summer/autumn (Figure S4 & S5). We further explore this newly-resolved seaonality by focusing on the Subtropical North Pacific, which was the subject of prior studies of eddy seasonality (Qiu et al., 2014).

Eddy dynamics from NeurOST are strongly seasonal in the Subtropical North Pacific, with enstrophy (the variance of vorticity) peaking in winter/spring implying intensified small-scale eddies (Figure 5a). This strong wintertime peak in enstrophy in NeurOST is qualitatively consistent with submesoscale-resolving simulations (Qiu et al., 2014). The seasonality of small-scale eddies is corroborated by the KE wavenumber spectrum (S.I. S1.13) that has a shallower slope ($\approx k^{-2}$) in winter and spring than in summer and autumn ($\approx k^{-3}$) (Figure 5b), meaning energy is more concentrated at small scales in winter and spring. Notably, the peak in KE for small-scales (<125km) leads that for larger scales by two months (Figure 5c). It has been hypothesized that the delayed large-scale KE peak may partly be driven by an upscale KE cascade from submesoscales, which are most energetic during winter (Sasaki et al., 2014; Qiu et al., 2014). However, this hypothesis has not been confirmed using observations since low-resolution products like DUACS fail to resolve the small-scale eddies that proliferate in winter/spring (Figure 5a,c), and hence underestimate the KE cascade (Arbic et al., 2013).

The KE cascade from NeurOST is upscale throughout the mesoscale range in the Subtropical North Pacific, has a strong springtime peak, and is dramatically stronger than in DUACS (Figure 5d). Although some KE sources and sinks cannot be derived

from surface currents (S.I. S1.12), the magnitude of the cascade appears more than sufficient to drive the increase in large-scale KE observed over winter/spring (Figure 5e). In contrast, the overly smooth DUACS product significantly underestimates the springtime KE cascade, obscuring the seasonality of the cascade and its role in driving the large-scale peak (Figure 5e). The cascade also appears to play a crucial role in driving large-scale seasonality in other subtropical regions (Figure S6). At scales resolved in our study, there are no ground-truth data for the KE cascade to compare against (Yoo et al., 2018; Naveira Garabato et al., 2022; Balwada et al., 2022), but recent studies of along-track altimetry provide additional indirect evidence for the seasonal upscale KE cascade observed here (Steinberg et al., 2022; Lawrence & Callies, 2022; Schubert et al., 2023). Note that in western boundary currents, the lateral KE advection appears to dominate the cascade (Figure S6), and there is likely a substantial energy injection by instabilities of large-scale currents that cannot be diagnosed from SSH.

## 4 Conclusions

Our high-resolution SSH maps generated using deep learning represent a large stride forward for the global observation of ocean eddy dynamics, providing state-of-the-art global surface currents. Trained on real-world observations alone, NeurOST allows to diagnose eddy dynamics with greater physical realism than from existing altimetry products. NeurOST revealed the crucial role of non-linear eddy dynamics and their associated KE cascade in driving the seasonality of mesoscale eddies in many parts of the global ocean, highlighting the importance of resolving small-scale eddy dynamics in ocean models. Alongside this manuscript, we publish a NeurOST SSH product (Martin, 2024a) to facilitate future studies of eddy dynamics and the impacts of eddies on climate and marine ecosystems.

Despite the improved resolution of NeurOST, it does not yet resolve submesoscale eddies, smoothing scales below $O$(100km) (Table S4). Hence, the strength of the upscale cascade is likely still underestimated (Figure S7), and the potential presence of the downscale cascade at submesoscales cannot be quantified. The recently launched Surface Water and Ocean Topography (SWOT) satellite, the first wide-swath altimeter (Morrow et al., 2019; Fu et al., 2024), provides unprecedented 2D submesoscale-resolving SSH snapshots that could help characterize the KE cascade in the submesoscale range (Klein et al., 2019; Carli et al., 2023). However, SWOT observations present new challenges for inferring currents from SSH in the presence of unbalanced submesoscale SSH variability and the mismatch between the fast-evolving submesoscale dynamics and SWOT's long orbital return times (Gaultier et al., 2016; Torres et al., 2018). Deep learning methods to address these issues are under development and show promising results (Febvre et al., 2022; Wang et al., 2022; Gao et al., 2024). As satellite oceanography enters a new submesoscale-resolving era (Morrow et al., 2019; Fu et al., 2024), further development of deep learning methods will be crucial to best monitor surface currents and other essential climate variables, like SST (Goh et al., 2023; Agabin et al., 2024).

## 5 Open Research

The NeurOST maps for 2019 with 1 satellite altimeter withheld for validation are available (Martin, 2024c). A longer time-series of NeurOST maps using all available altimeters intended for users is available through NASA PO.DAAC (Martin, 2024a). We used MUR SST data from PO.DAAC (JPL MUR MEaSUREs Project, 2015) and the altimeter, surface drifter observations, and GLORYS reanalysis data from CMEMS (E.U. Copernicus Marine Service Information (CMEMS), 2024b, 2024a, 2024c, 2024d). Ocean Data Challenges for global SSH mapping (`https://github.com/ocean-data-challenges/2023a_SSH_mapping_OSE`) and for the Gulf Stream Extension (`https://github.com/ocean-data-challenges/2021a_SSH_mapping_OSE`) are on GitHub. Gulf Stream SSH maps

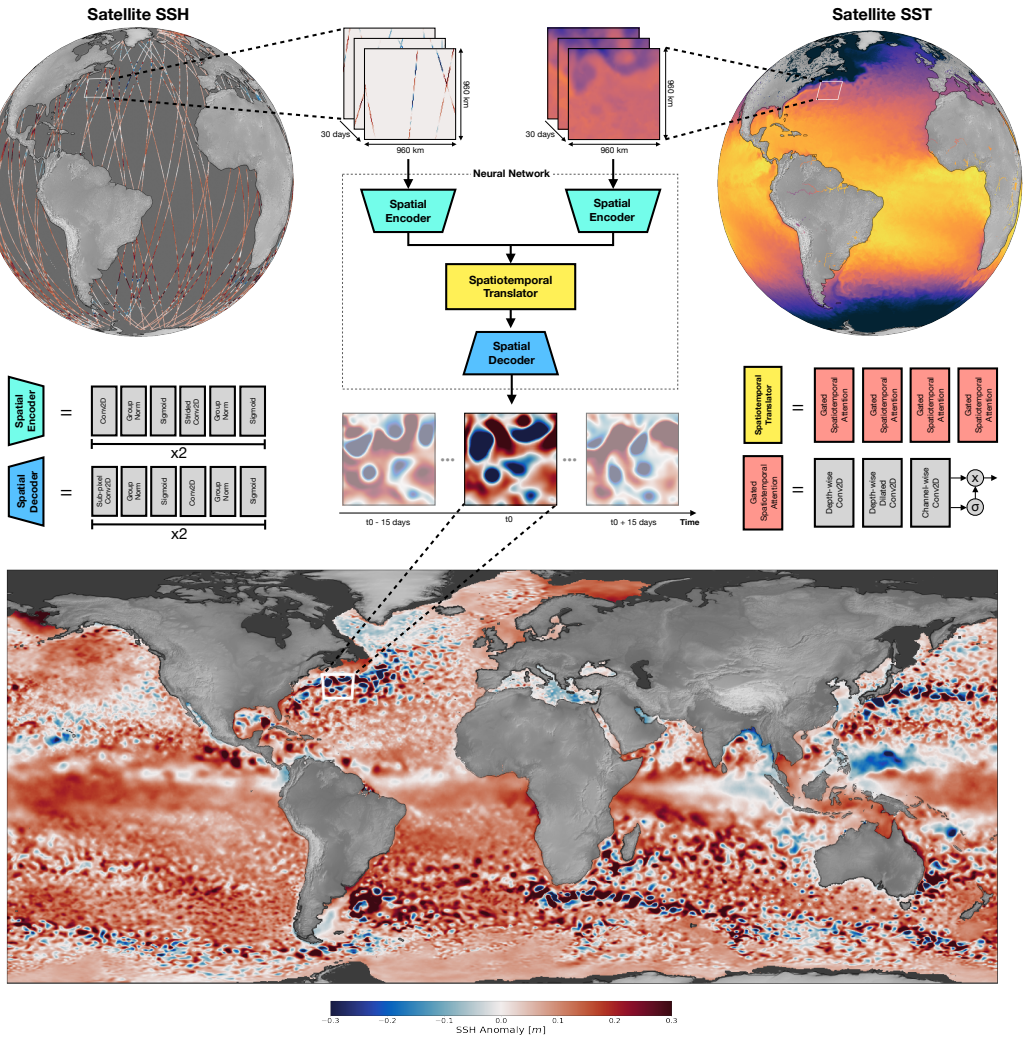


**Figure 1.** Schematic of NeurOST SSH-SST method for mapping SSH from satellite altimetry and SST.

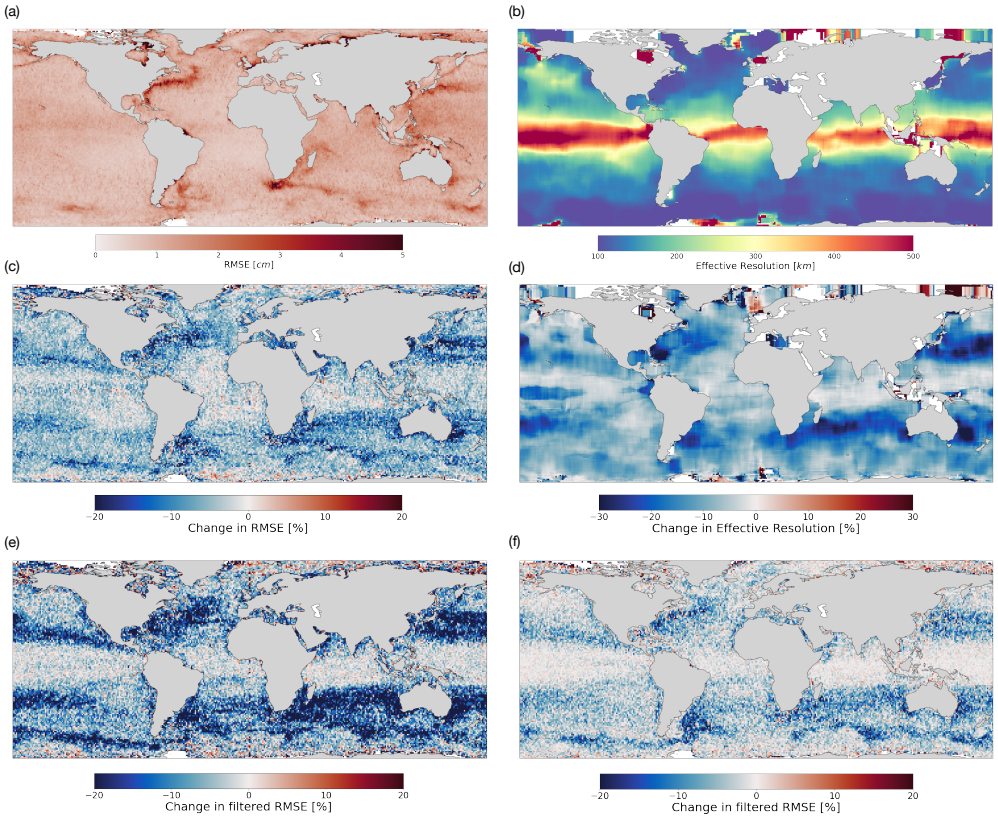


**Figure 2.** (a) RMSE of NeurOST SSH-SST compared to withheld altimeter. (b) Smallest resolved wavelengths (effective resolution) of NeurOST SSH-SST. (c) Change in RMSE of NeurOST SSH-SST compared to DUACS. (d) Change in effective resolution of NeurOST SSH-SST compared to DUACS. (e) Change in RMSE of small-scale (70-250km) signals of NeurOST SSH-SST compared to DUACS. (f) Change in RMSE of small-scale signals of NeurOST SSH-SST compared to NeurOST SSH. Blue colors indicate a relative decrease in error in panels c-f.

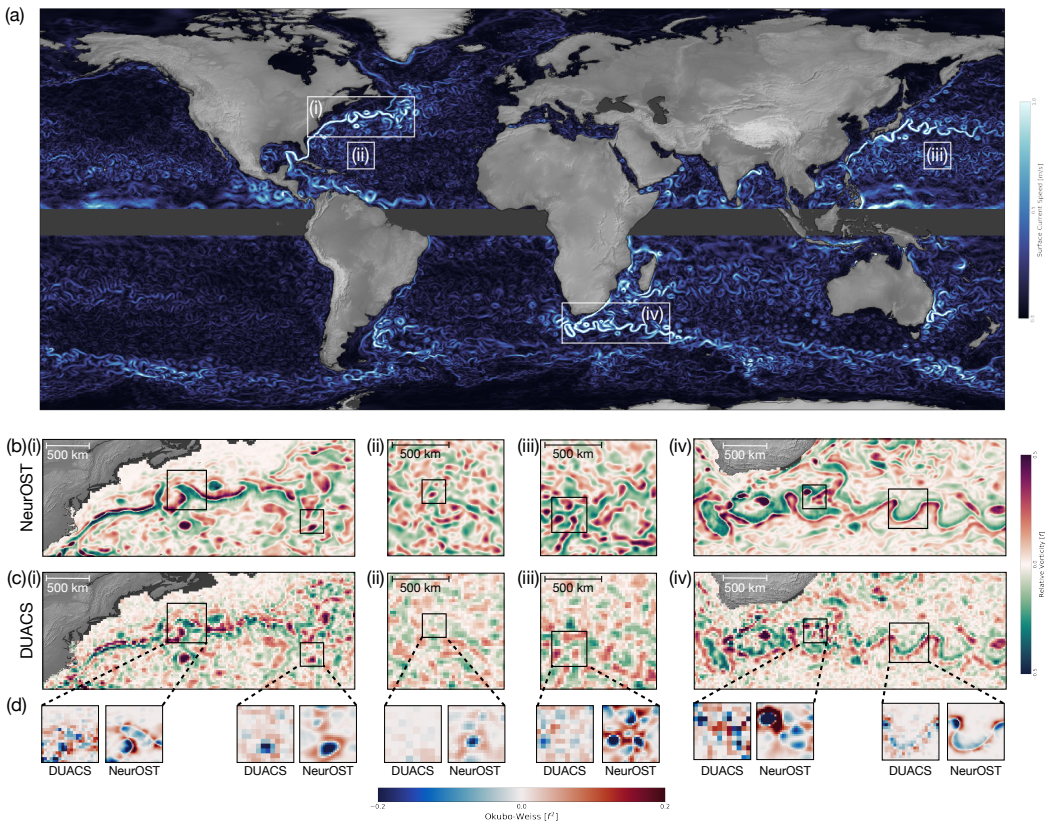


**Figure 3.** (a) Surface geostrophic current speed on March 1st 2019 derived from SSH maps made using NeurOST SSH-SST. (b) Relative vorticity from NeurOST SSH-SST. (c) Relative vorticity from DUACS. (d) Zoomed insets of Okubo-Weiss quantity for DUACS and NeurOST SSH-SST.

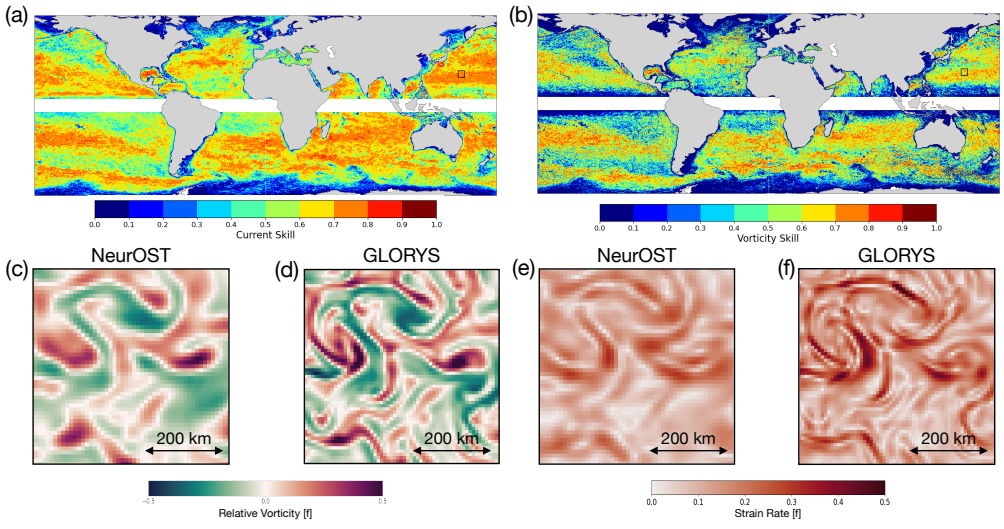


**Figure 4.** NeurOST SSH-SST reconstruction skill (explained variance) in GLORYS OSSE for (a) surface geostrophic currents and (b) vorticity. Snapshots of (c, d) vorticity and (e, f) strain from Subtropical North Pacific (boxed region in a and b) for NeurOST and GLORYS on Feb 26th 2019.

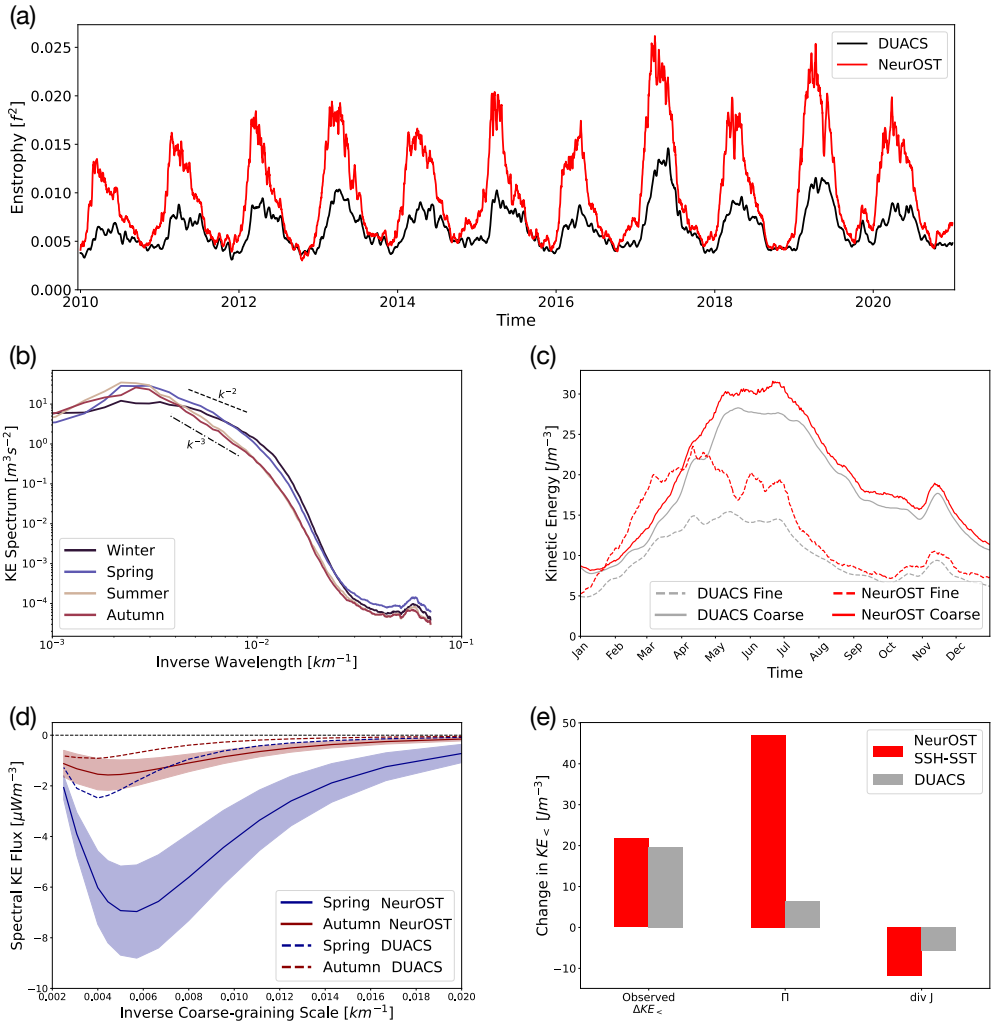


**Figure 5.** (a) Enstrophy time-series in the Subtropical North Pacific for NeurOST SSH-SST and DUACS. (b) KE spectra from NeurOST SSH-SST split by season. (c) Time-series of coarse- and fine-scale KE (above and below 125km coarse-graining scale respectively) from NeurOST SSH-SST (red) and DUACS (grey). (d) KE cascade from NeurOST SSH-SST maps for the seasons of maximum (Spring) and minimum (Autumn) upscale cascade (solid line: mean, shading: standard deviation). Dashed lines are the mean cascades from DUACS. (e) Change in coarse-scale KE ($KE_<$) from the winter-time minimum to the summer-time maximum compared to the diagnosed contributions of the KE cascade ($-\int \Pi dt$), and the spatial transport of coarse-scale KE ($-\int \nabla \cdot J dt$) from NeurOST SSH-SST (red) and DUACS (grey) (S.I. S1.12).

for Febvre et al. (2024) and Archambault et al. (2023) are at `https://doi.org/10.5281/zenodo.8064113` and `https://gitlab.lip6.fr/archambault/visapp2023` respectively.

NeurOST code is available (Martin, 2024b) and for coarse-graining we used FlowSieve (Storer & Aluie, 2023).

**Acknowledgments**

The research was funded by NASA Grant 80NSSC21K1187. P.K. acknowledges support from the SWOT Science Team and the QuikSCAT mission. We thank the creators of the Ocean Data Challenges, especially Sammy Metref and Maxime Ballarotta. We acknowledge helpful discussions with Steven Brunton, Jinbo Wang, Brian Arbic, Quentin Febvre, Tom Farrar, J. Xavier Prochaska, Peter Cornillon, and Christian Buckingham. Computational resources supporting this work were provided by the NASA High-End Computing (HEC) Program through the NASA Advanced Supercomputing (NAS) Division at Ames Research Center. We thank Julian Mak and two anonymous reviewers for helping to improve the manuscript.

## References


Agabin, A., Prochaska, J. X., Cornillon, P. C., & Buckingham, C. E. (2024). Mitigating masked pixels in a climate-critical ocean dataset. *Remote Sensing*, *16*(13).

Ajayi, A., Le Sommer, J., Chassignet, E. P., Molines, J.-M., Xu, X., Albert, A., & Dewar, W. (2021). Diagnosing cross-scale kinetic energy exchanges from two submesoscale permitting ocean models. *Journal of Advances in Modeling Earth Systems*, *13*(6), e2019MS001923.

Aluie, H., Hecht, M., & Vallis, G. K. (2018). Mapping the energy cascade in the North Atlantic Ocean: The coarse-graining approach. *Journal of Physical Oceanography*, *48*(2), 225–244.

Arbic, B. K., Polzin, K. L., Scott, R. B., Richman, J. G., & Shriver, J. F. (2013). On eddy viscosity, energy cascades, and the horizontal resolution of gridded satellite altimeter products. *Journal of Physical Oceanography*, *43*(2), 283–300.

Archambault, T., Filoche, A., Charantonis, A., & Béréziat, D. (2024). Pre-training and fine-tuning attention based encoder decoder improves sea surface height multi-variate inpainting. In *VISAPP.*

Archambault, T., Filoche, A., Charantonnis, A., & Béréziat, D. (2023). Multimodal unsupervised spatio-temporal interpolation of satellite ocean altimetry maps. In *VISAPP.*

Ballarotta, M., Metref, S., Albery, A., Cosme, E., Beauchamp, M., & Le Guillou, F. (2021). *Ocean data challenges.* (`https://github.com/ocean-data-challenges/2021a_SSH_mapping_OSE`)

Ballarotta, M., Ubelmann, C., Pujol, M.-I., Taburet, G., Fournier, F., Legeais, J.-F., ... others (2019). On the resolutions of ocean altimetry maps. *Ocean Science*, *15*(4), 1091–1109.

Ballarotta, M., Ubelmann, C., Veillard, P., Prandi, P., Etienne, H., Mulet, S., ... Picot, N. (2023). Improved global sea surface height and current maps from remote sensing and in situ observations. *Earth System Science Data*, *15*(1), 295–315.

Balwada, D., Xie, J.-H., Marino, R., & Feraco, F. (2022). Direct observational evidence of an oceanic dual kinetic energy cascade and its seasonality. *Science Advances*, *8*(41), eabq2566.

Beauchamp, M., Febvre, Q., Georgenthum, H., & Fablet, R. (2022). 4DVarNet-SSH: end-to-end learning of variational interpolation schemes for nadir and wide-swath satellite altimetry. *Geoscientific Model Development Discussions*, *2022*, 1–37.

Buongiorno Nardelli, B., Cavaliere, D., Charles, E., & Ciani, D. (2022). Super-resolving ocean dynamics from space with computer vision algorithms. *Remote Sensing*, *14*(5), 1159.

Callaham, J. L., Maeda, K., & Brunton, S. L. (2019). Robust flow reconstruction from limited measurements via sparse representation. *Physical Review Fluids*, *4*(10), 103907.

Cao, Y., Dong, C., Stegner, A., Bethel, B. J., Li, C., Dong, J., ... Yang, J. (2023). Global sea surface cyclogeostrophic currents derived from satellite altimetry data. *Journal of Geophysical Research: Oceans*, *128*(1), e2022JC019357.

Carli, E., Morrow, R., Vergara, O., Chevrier, R., & Renault, L. (2023). Ocean 2D eddy energy fluxes from small mesoscale processes with SWOT. *Ocean Science*, *19*(5), 1413–1435.

Chelton, D. B., Ries, J. C., Haines, B. J., Fu, L.-L., & Callahan, P. S. (2001). Satellite altimetry. In *International geophysics* (Vol. 69, pp. 1–ii). Elsevier.

Cornillon, P. C., Firing, E., Thompson, A., Ivanov, L., Kamenkovich, I., Buckingham, C. E., & Afanasyev, Y. (2019). Oceans. In B. Galperin & P. Read

(Eds.), *Zonal jets phenomenology, genesis, and physics* (p. 46 - 71). Cambridge University Press. doi: 10.1017/9781107358225.003

Dufau, C., Orsztynowicz, M., Dibarboure, G., Morrow, R., & Le Traon, P.-Y. (2016). Mesoscale resolution capability of altimetry: Present and future. *Journal of Geophysical Research: Oceans*, *121*(7), 4910–4927.

E.U. Copernicus Marine Service Information (CMEMS). (2024a). *Global ocean along track l 3 sea surface heights NRT.* Retrieved from `https://doi.org/10.48670/moi-00147` (Accessed on 07-04-2024)

E.U. Copernicus Marine Service Information (CMEMS). (2024b). *Global ocean along track l 3 sea surface heights reprocessed 1993 ongoing tailored for data assimilation.* Retrieved from `https://doi.org/10.48670/moi-00146` (Accessed on 07-04-2024)

E.U. Copernicus Marine Service Information (CMEMS). (2024c). *Global ocean-delayed mode in situ observations of surface (drifters, HFR) and sub-surface (vessel-mounted adcps) water velocity.* Retrieved from `https://doi.org/10.17882/86236` (Accessed on 07-04-2024)

E.U. Copernicus Marine Service Information (CMEMS). (2024d). *Global ocean physics reanalysis.* Retrieved from `https://doi.org/10.48670/moi-00021` (Accessed on 07-04-2024)

Fablet, R., Amar, M. M., Febvre, Q., Beauchamp, M., & Chapron, B. (2021). End-to-end physics-informed representation learning for satellite ocean remote sensing data: Applications to satellite altimetry and sea surface currents. *ISPRS Annals of Photogrammetry, Remote Sensing & Spatial Information Sciences*(3).

Fablet, R., Febvre, Q., & Chapron, B. (2023). Multimodal 4DVarNets for the reconstruction of sea surface dynamics from SST-SSH synergies. *IEEE Transactions on Geoscience and Remote Sensing*.

Febvre, Q., Fablet, R., Le Sommer, J., & Ubelmann, C. (2022). Joint calibration and mapping of satellite altimetry data using trainable variational models. In *ICASSP 2022-2022 IEEE International Conference on Acoustics, Speech and Signal Processing (ICASSP)* (pp. 1536–1540).

Febvre, Q., Le Sommer, J., Ubelmann, C., & Fablet, R. (2024). Training neural mapping schemes for satellite altimetry with simulation data. *Journal of Advances in Modeling Earth Systems*, *16*(7), e2023MS003959. Retrieved from `https://agupubs.onlinelibrary.wiley.com/doi/abs/10.1029/2023MS003959` doi: https://doi.org/10.1029/2023MS003959

Ferrari, R., & Wunsch, C. (2009). Ocean circulation kinetic energy: Reservoirs, sources, and sinks. *Annual Review of Fluid Mechanics*, *41*, 253–282.

Fu, L.-L., Pavelsky, T., Cretaux, J.-F., Morrow, R., Farrar, J. T., Vaze, P., ... others (2024). The Surface Water and Ocean Topography mission: A breakthrough in radar remote sensing of the ocean and land surface water. *Geophysical Research Letters*, *51*(4), e2023GL107652.

Gao, Z., Chapron, B., Ma, C., Fablet, R., Febvre, Q., Zhao, W., & Chen, G. (2024). A deep learning approach to extract balanced motions from sea surface height snapshot. *Geophysical Research Letters*, *51*(7), e2023GL106623.

Gaultier, L., Ubelmann, C., & Fu, L.-L. (2016). The challenge of using future SWOT data for oceanic field reconstruction. *Journal of Atmospheric and Oceanic Technology*, *33*(1), 119–126.

Goh, E., Yepremyan, A. R., Wang, J., & Wilson, B. (2023). MAESSTRO: Masked autoencoders for sea surface temperature reconstruction under occlusion. *EGUsphere [pre-print]*, *2023*, 1–20.

Hoskins, B. J. (1982). The mathematical theory of frontogenesis. *Annual Review of Fluid Mechanics*, *14*(1), 131–151.

Isern-Fontanet, J., Chapron, B., Lapeyre, G., & Klein, P. (2006). Potential use of microwave sea surface temperatures for the estimation of ocean currents. *Geo-*

*physical Research Letters*, *33*(24).

Isern-Fontanet, J., Shinde, M., & González-Haro, C. (2014). On the transfer function between surface fields and the geostrophic stream function in the Mediterranean Sea. *Journal of Physical Oceanography*, *44*(5), 1406–1423.

Jayne, S. R., & Marotzke, J. (2002). The oceanic eddy heat transport. *Journal of Physical Oceanography*, *32*(12), 3328–3345.

JPL MUR MEaSUREs Project. (2015). *GHRSST level 4 MUR global foundation sea surface temperature analysis. ver. 4.1.* Retrieved from `https://doi.org/10.5067/GHGMR-4FJ04` (Accessed on 07-04-2024)

Klein, P., Lapeyre, G., Siegelman, L., Qiu, B., Fu, L.-L., Torres, H., ... Le Gentil, S. (2019). Ocean-scale interactions from space. *Earth and Space Science*, *6*(5), 795–817.

Kugusheva, A., Bull, H., Moschos, E., Ioannou, A., Le Vu, B., & Stegner, A. (2024). Ocean satellite data fusion for high-resolution surface current maps. *Remote Sensing*, *16*(7), 1182.

Lagerloef, G. S., Mitchum, G. T., Lukas, R. B., & Niiler, P. P. (1999). Tropical Pacific near-surface currents estimated from altimeter, wind, and drifter data. *Journal of Geophysical Research: Oceans*, *104*(C10), 23313–23326.

Lawrence, A., & Callies, J. (2022). Seasonality and spatial dependence of mesoscale and submesoscale ocean currents from along-track satellite altimetry. *Journal of Physical Oceanography*, *52*(9), 2069–2089.

Le Guillou, F., Gaultier, L., Ballarotta, M., Metref, S., Ubelmann, C., Cosme, E., & Rio, M.-H. (2023). Regional mapping of energetic short mesoscale ocean dynamics from altimetry: performances from real observations. *Ocean Science*, *19*(5), 1517–1527.

Le Guillou, F., Metref, S., Cosme, E., Ubelmann, C., Ballarotta, M., Le Sommer, J., & Verron, J. (2021). Mapping altimetry in the forthcoming SWOT era by back-and-forth nudging a one-layer quasigeostrophic model. *Journal of Atmospheric and Oceanic Technology*, *38*(4), 697–710.

Lellouche, J.-M., Greiner, E., Bourdallé-Badie, R., Garric, G., Melet, A., Drévillon, M., ... Le Traon, P.-Y. (2021). The copernicus global 1/12 oceanic and sea ice GLORYS12 reanalysis. *Frontiers in Earth Science*, *9*, 698876.

Le Traon, P., Nadal, F., & Ducet, N. (1998). An improved mapping method of multisatellite altimeter data. *Journal of Atmospheric and Oceanic Technology*, *15*(2), 522–534.

Manucharyan, G. E., Siegelman, L., & Klein, P. (2021). A deep learning approach to spatiotemporal sea surface height interpolation and estimation of deep currents in geostrophic ocean turbulence. *Journal of Advances in Modeling Earth Systems*, *13*(1), e2019MS001965.

Martin, S. A. (2024a). *Daily NeurOST L4 sea surface height and surface geostrophic currents.* Retrieved from `https://doi.org/10.5067/NEURO-STV24` (Accessed on 07-08-2024)

Martin, S. A. (2024b). *Global DL SSH.* Retrieved from `https://doi.org/10.5281/zenodo.11099094` (Accessed on 01-05-2024)

Martin, S. A. (2024c). *Simvp global SSH maps 2019.* Retrieved from `https://doi.org/10.7910/DVN/H4HQGD` (Accessed on 07-04-2024)

Martin, S. A., Manucharyan, G. E., & Klein, P. (2023). Synthesizing sea surface temperature and satellite altimetry observations using deep learning improves the accuracy and resolution of gridded sea surface height anomalies. *Journal of Advances in Modeling Earth Systems*, *15*(5), e2022MS003589.

Metref, S., & Ballarotta, M. (2023). *Ocean data challenges.* (`https://github.com/ocean-data-challenges/2023a_SSH_mapping_OSE`)

Metref, S., Ballarotta, M., Le Sommer, J., Cosme, E., Albert, A., Beauchamp, M., ... Febvre, Q. (2023). *Ocean data challenges.* (`https://ocean-data-challenges.github.io/`)

Morrow, R., Fu, L.-L., Ardhuin, F., Benkiran, M., Chapron, B., Cosme, E., ... others (2019). Global observations of fine-scale ocean surface topography with the surface water and ocean topography (SWOT) mission. *Frontiers in Marine Science*, *6*, 232.

Naveira Garabato, A. C., Yu, X., Callies, J., Barkan, R., Polzin, K. L., Frajka-Williams, E. E., ... Griffies, S. M. (2022). Kinetic energy transfers between mesoscale and submesoscale motions in the open ocean's upper layers. *Journal of Physical Oceanography*, *52*(1), 75–97.

Penven, P., Halo, I., Pous, S., & Marié, L. (2014). Cyclogeostrophic balance in the Mozambique Channel. *Journal of Geophysical Research: Oceans*, *119*(2), 1054–1067.

Qiu, B., Chen, S., Klein, P., Sasaki, H., & Sasai, Y. (2014). Seasonal mesoscale and submesoscale eddy variability along the north pacific subtropical countercurrent. *Journal of Physical Oceanography*, *44*(12), 3079–3098.

Rio, M.-H., Mulet, S., & Picot, N. (2014). Beyond GOCE for the ocean circulation estimate: Synergetic use of altimetry, gravimetry, and in situ data provides new insight into geostrophic and ekman currents. *Geophysical Research Letters*, *41*(24), 8918–8925.

Rio, M.-H., Santoleri, R., Bourdalle-Badie, R., Griffa, A., Piterbarg, L., & Taburet, G. (2016). Improving the altimeter-derived surface currents using high-resolution sea surface temperature data: a feasability study based on model outputs. *Journal of Atmospheric and Oceanic Technology*, *33*(12), 2769–2784.

Sasaki, H., Klein, P., Qiu, B., & Sasai, Y. (2014). Impact of oceanic-scale interactions on the seasonal modulation of ocean dynamics by the atmosphere. *Nature Communications*, *5*(1), 5636.

Schubert, R., Gula, J., Greatbatch, R. J., Baschek, B., & Biastoch, A. (2020). The submesoscale kinetic energy cascade: Mesoscale absorption of submesoscale mixed layer eddies and frontal downscale fluxes. *Journal of Physical Oceanography*, *50*(9), 2573–2589.

Schubert, R., Vergara, O., & Gula, J. (2023). The open ocean kinetic energy cascade is strongest in late winter and spring. *Communications Earth & Environment*, *4*(1), 450.

Scott, R. B., & Wang, F. (2005). Direct evidence of an oceanic inverse kinetic energy cascade from satellite altimetry. *Journal of Physical Oceanography*, *35*(9), 1650–1666.

Siegelman, L., Klein, P., Rivière, P., Thompson, A. F., Torres, H. S., Flexas, M., & Menemenlis, D. (2020). Enhanced upward heat transport at deep submesoscale ocean fronts. *Nature Geoscience*, *13*(1), 50–55.

Sinha, A., & Abernathey, R. (2021). Estimating ocean surface currents with machine learning. *Frontiers in Marine Science*, *8*, 672477.

Steinberg, J. M., Cole, S. T., Drushka, K., & Abernathey, R. P. (2022). Seasonality of the mesoscale inverse cascade as inferred from global scale-dependent eddy energy observations. *Journal of Physical Oceanography*, *52*(8), 1677–1691.

Storer, B. A., & Aluie, H. (2023). FlowSieve: A coarse-graining utility for geophysical flows on the sphere. *Journal of Open Source Software*, *8*(84), 4277.

Storer, B. A., Buzzicotti, M., Khatri, H., Griffies, S. M., & Aluie, H. (2022). Global energy spectrum of the general oceanic circulation. *Nature Communications*, *13*(1), 5314.

Storer, B. A., Buzzicotti, M., Khatri, H., Griffies, S. M., & Aluie, H. (2023). Global cascade of kinetic energy in the ocean and the atmospheric imprint. *Science Advances*, *9*(51), eadi7420.

Taburet, G., Sanchez-Roman, A., Ballarotta, M., Pujol, M.-I., Legeais, J.-F., Fournier, F., ... Dibarboure, G. (2019). DUACS DT2018: 25 years of reprocessed sea level altimetry products. *Ocean Science*, *15*(5), 1207–1224.

Taylor, J. R., & Thompson, A. F. (2023). Submesoscale dynamics in the upper

ocean. *Annual Review of Fluid Mechanics*, *55*, 103–127.

Thiria, S., Sorror, C., Archambault, T., Charantonis, A., Bereziat, D., Mejia, C., ... Crépon, M. (2023). Downscaling of ocean fields by fusion of heterogeneous observations using deep learning algorithms. *Ocean Modelling*, *182*, 102174.

Torres, H. S., Klein, P., Menemenlis, D., Qiu, B., Su, Z., Wang, J., ... Fu, L.-L. (2018). Partitioning ocean motions into balanced motions and internal gravity waves: A modeling study in anticipation of future space missions. *Journal of Geophysical Research: Oceans*, *123*(11), 8084–8105.

Ubelmann, C., Carrere, L., Durand, C., Dibarboure, G., Faugère, Y., Ballarotta, M., ... Lyard, F. (2022). Simultaneous estimation of ocean mesoscale and coherent internal tide sea surface height signatures from the global altimetry record. *Ocean Science*, *18*(2), 469–481.

Ubelmann, C., Dibarboure, G., Gaultier, L., Ponte, A., Ardhuin, F., Ballarotta, M., & Faugère, Y. (2021). Reconstructing ocean surface current combining altimetry and future spaceborne Doppler data. *Journal of Geophysical Research: Oceans*, *126*(3), e2020JC016560.

Ubelmann, C., Klein, P., & Fu, L.-L. (2015). Dynamic interpolation of sea surface height and potential applications for future high-resolution altimetry mapping. *Journal of Atmospheric and Oceanic Technology*, *32*(1), 177–184.

Uchida, T., Abernathey, R., & Smith, S. (2017). Seasonality of eddy kinetic energy in an eddy permitting global climate model. *Ocean Modelling*, *118*, 41–58.

Wang, H., Grisouard, N., Salehipour, H., Nuz, A., Poon, M., & Ponte, A. L. (2022). A deep learning approach to extract internal tides scattered by geostrophic turbulence. *Geophysical Research Letters*, *49*(11), e2022GL099400.

Wunsch, C. (1999). Where do ocean eddy heat fluxes matter? *Journal of Geophysical Research: Oceans*, *104*(C6), 13235–13249.

Xiao, Q., Balwada, D., Jones, C. S., Herrero-González, M., Smith, K. S., & Abernathey, R. (2023). Reconstruction of surface kinematics from sea surface height using neural networks. *Journal of Advances in Modeling Earth Systems*, *15*(10), e2023MS003709.

Yoo, J. G., Kim, S. Y., & Kim, H. S. (2018). Spectral descriptions of submesoscale surface circulation in a coastal region. *Journal of Geophysical Research: Oceans*, *123*(6), 4224–4249.

Zhang, Z., Wang, W., & Qiu, B. (2014). Oceanic mass transport by mesoscale eddies. *Science*, *345*(6194), 322–324.

# Supporting Information for "Deep Learning Improves Global Satellite Observations of Ocean Eddy Dynamics"

Scott A. Martin[1], Georgy E. Manucharyan[1], and Patrice Klein[2,3]

[1]School of Oceanography, University of Washington, Seattle, WA, USA

[2]Jet Propulsion Laboratory, California Institute of Technology, Pasadena, CA, USA

[3]Laboratoire de Météorologie Dynamique, École Normale Supérieure, Paris, France

## Contents of this file

1. Text S1 to S2

2. Tables S1 to S4

3. Figures S1 to S11

## Additional Supporting Information (Files uploaded separately)

1. Captions for Movies S1 & S2

July 12, 2024, 6:20pm

# 1. Text S1: Extended Methods

## 1.1. Sea surface height and surface geostrophic currents

At large temporal and spatial scales, ocean currents are approximately in geostrophic balance (Vallis, 2017), meaning that currents arrange themselves such that the horizontal pressure gradient force is balanced by the Coriolis force. Surface pressure in the ocean can be directly related to sea surface height anomaly (SSH), allowing surface current velocity to be estimated from satellite altimeter observations of SSH. The surface currents are proportional to the spatial gradients of the SSH field

$$(u_g, v_g) = \frac{g}{f}\left(-\frac{\partial \eta}{\partial y}, \frac{\partial \eta}{\partial x}\right), \tag{1}$$

where $u_g$ and $v_g$ are the Eastward and Northward geostrophic surface currents respectively, $g$ is the acceleration due to gravity, $\eta$ is the SSH, $f$ is the local Coriolis frequency, and $x$ and $y$ are zonal and meridional coordinates respectively. This relation breaks down near the Equator where $f$ approaches zero, so we do not calculate surface geostrophic currents within the equatorial band (5°S to 5°N).

Geostrophy breaks down at smaller scales where the impact of non-linear advection becomes significant, and does not account for wind-induced Ekman currents. Empirical corrections can be made to geostrophy at the Equator (Lagerloef et al., 1999), to estimate Ekman currents (Rio et al., 2014), and to include the effect of non-linear advection through cyclo-geostrophic balance (Penven et al., 2014; Cao et al., 2023). Ekman currents and equatorial dynamics are not the focus of this study, but since cyclo-geostrophy is pertinent for mesoscale eddies we do assess the sensitivity of our results to correcting

for this component using the iterative method proposed in Penven et al. (2014). The cyclo-geostrophic correction leads to a marginally improved surface current RMSE when evaluated using drifters compared to conventional geostrophy but the change is typically well below 10%, highlighting the relatively small impact of this correction at the scales resolved here (S.I. Figure 2). Further, we find that the KE cascade diagnosed from both NeurOST and GLORYS changes very little when the cyclo-geostrophic correction is applied (S.I. Figure 2). The near-perfect agreement between the GLORYS cyclo-geostrophic KE cascade and that from the GLORYS 15m currents highlights the pertinence of this empirical correction, but the small correction to the currents highlights that they are to leading order geostrophic.

### 1.2. Satellite datasets

The along-track SSH observations used in this study are those processed by the Data Unification and Altimeter Combination System (DUACS) and distributed by the Copernicus Marine Environmental Service (CMEMS) (E.U. Copernicus Marine Service Information (CMEMS), 2024b, 2024a). Specifically, we use the unfiltered, Level 3 sea level anomaly observations. At Level 3, the observations have been corrected for atmospheric effects, the barotropic tide has been removed, and the data has been adjusted to ensure consistency between the different altimeter missions.

We use the Multi-scale Ultra-high Resolution (MUR) SST analysis product to provide a gridded estimate of SST as an additional predictor variable in the mapping of SSH that combines observations from a wide range of satellite infrared and microwave radiometer observations (JPL MUR MEaSUREs Project, 2015; Chin et al., 2017). While this product

is distributed on a 1/100th degree grid, the spatial scales resolved vary in space and time due to satellite sampling and cloud cover.

### 1.3. Formulating SSH interpolation as a self-supervised deep learning problem

After appropriate data pre-processing, SSH interpolation can be viewed as a video inpainting problem with an extremely high missing pixel rate ($\sim 90\%$) (Manucharyan et al., 2021; Martin et al., 2023; Fablet et al., 2021). We first extract satellite altimeter SSH observations in some restricted spatiotemporal subdomain within which we seek to estimate the full SSH field. This subdomain is discretized into a regular grid in space and time onto which the observations are bin-averaged; empty voxels are padded with zeroes. This data can now be considered as a heavily-masked video, and our objective is to predict the corresponding full, unmasked video using a deep learning neural network. The objective minimized during training is the mean squared error (MSE) between the prediction and the ground-truth. When training on real-world altimetry observations, there is no full unmasked ground-truth dataset to use during training. We overcome this by randomly withholding some of the altimetry observations from the input and calculating the MSE only at the locations of these withheld observations (Martin et al., 2023). Alternative loss functions and regularization terms (e.g. the along-track derivative regularizations used in Martin et al. (2023) and explored further in Archambault, Filoche, Charantonis, Béréziat, and Thiria (2024) or along-track spectral regularizations) may yield further mapping improvements in future studies but we restrict ourselves to MSE here due to the computational expense of iterating on loss function choice for global mapping. Co-located estimates of gridded SST are used as an extra predictor variable

by averaging them onto the same local grid and presenting this (unmasked) video as an additional input to the neural network. The dimensions of the local grid on which we map SSH were chosen to be 128x128 in the spatial domain with 7.5km grid resolution (latitude, longitude coordinates are first projected onto a local orthonormal grid to avoid distortion), and 30 frames in the temporal domain with 1 day grid resolution. Rationalization and validation of these choices is given in our previous study (Martin et al., 2023). To train our network, we generated a training dataset of 1 million local subdomains centred on random points in space and time throughout the Global Ocean. The data are split in the temporal domain to ensure well-separated training, validation, and testing datasets, with 2019 being withheld for testing, and the remaining years from 2010-2022 split into non-overlapping training and validation periods (S.I. Figure 2).

The mapping errors grow away from the centre of the local spatiotemporal grid due the omission of observations outside the local subdomain, therefore to produce the optimal reconstruction we use only the middle day of the predicted time-series during inference and points close to the edge of the subdomain are given low weight in our algorithm for merging subdomain reconstructions to produce a global SSH estimate 1.5.

### 1.4. Deep learning neural network architecture

After formulating SSH interpolation as discussed above, we are to free to use any sequence-to-sequence video prediction model from the extensive computer vision literature. To ensure we employed a state-of-the-art architecture, we chose the top-performing architecture on the Moving MNIST video prediction benchmark (Srivastava et al., 2015) at the time of our study, SimVP (Gao et al., 2022; Tan et al., 2022). SimVP is built

up of three modules: a spatial encoder that learns to encode each frame of the input independently in some lower-dimensional latent space, a temporal translator that learns both spatial and temporal dependencies from the latent space, and a spatial decoder that decodes the latent space into the predicted video frames. Unlike widely-used recurrent architectures, such as ConvLSTM (Shi et al., 2015), SimVP uses convolutional neural networks (CNNs) for all three modules. Our architecture is as described in Tan et al. (Tan et al., 2022), where the temporal translator module is a gated spatio-temporal attention translator, which uses large convolutional kernels to imitate the attention mechanism allowing the translator to adaptively select informative features from the latent space. Compared with Tan et al., we removed the skip connection from the first layer of the spatial encoder to the final layer of the spatial decoder since the extreme sparsity of the input SSH frames led to the appearance of artifacts in the output coinciding with the input altimeter tracks. To synthesize SSH and SST, we use a separate spatial encoder for each variable before concatenating the encoded SSH and SST in the channel dimension and passing this to the temporal translator. Except for the temporal translator, the architecture used here is similar to the ConvLSTM-based architecture used in our earlier regional SSH mapping study (Martin et al., 2023). During early testing we found SimVP to outperform ConvLSTM in global SSH reconstruction, which requires a more expressive architecture due to the diverse range of dynamical regimes, and its performance (when trained on global data) is comparable to our previously published values for ConvLSTM in the Gulf Stream despite the latter being trained exclusively on this region (S.I. Table 2). Each network was trained for 50 epochs using the OneCycle learning rate scheduling

policy, the Adam optimizer, and with drop-out and drop-path probabilities of 0.2 and 0.15 respectively which were selected after performing hyper-parameter optimization on 10% of the training data. Each training on the global training dataset took 7 days on a single node with four Nvidia V100 GPUs.

### 1.5. Merging subdomain reconstructions to create global SSH product

Our neural network predicts gridded SSH on subdomains of size 960x960km. To produce a global gridded SSH estimate we use the trained network to predict SSH on 5615 subdomains with centres chosen to be approximately equally spaced by a distance of 250km throughout the Global Ocean. There is therefore substantial overlap between neighbouring subdomains. To merge the subdomain reconstructions into a single global SSH estimate we use the kernel-weighted averaging method described in Appendix A of Callaham et al. (Callaham et al., 2019) and outlined below.

The global 2D SSH estimate, $\widehat{\mathbf{x}}$, defined on a regular 1/10th degree grid, is computed from the $k$ subdomain estimates through

$$\widehat{\mathbf{x}} = \sum_{i=1}^{k} \Phi_i \odot \widehat{\mathbf{x}}_i, \tag{2}$$

where $\Phi_i$ is a normalized weighting kernel for each subdomain, $\widehat{\mathbf{x}}_i$ are the subdomain SSH estimates, and $\odot$ denotes the Hadamard (i.e. element-wise) product between two matrices. Note that each $\widehat{\mathbf{x}}_i$ and $\Phi_i$ are filled with zeroes at all points covered by land or sea ice and at points lying outside the subdomain. All matrices were first regridded to the regular 1/10th degree grid from the original, irregular subdomain grid using bilinear interpolation. Each weighting kernel is taken to be a Gaussian centered on the the

corresponding subdomain

$$\Phi_i(\mathbf{r}) = \frac{1}{N(\mathbf{r})} \exp\left(-\frac{|\mathbf{r}-\mathbf{r}_i|^2}{L^2}\right), \tag{3}$$

where $\mathbf{r}$ is the position of the point being estimated, $\mathbf{r_i}$ is the position of the subdomain center, $L$ is the characteristic width of the Gaussian kernel, and $N(\mathbf{r})$ is a normalization factor chosen such that

$$N(\mathbf{r}) = \sum_{i=1}^{k} \Phi_i(\mathbf{r}). \tag{4}$$

The mapping errors in the subdomain reconstructions are expected to increase away from the center of the subdomain due to the omission of observations outside the subdomain in the mapping. Thus, for minimizing the error of the global estimate maximizing the number of subdomains is desirable. The choice to space the subdomains by 250km was made as the minimum spacing our computing resources would reasonably permit (merging the subdomain reconstructions for a single day takes $\sim$ 3 minutes per CPU worker at this spacing). Given this subdomain spacing, the value of $L$ was tuned so as to minimize the mapping error for the global estimate. We found the errors to be only weakly dependent on kernel width for widths within reasonable bounds, the results presented in the manuscript were obtained using $L = 250$km. All first- and second-order spatial derivatives of the SSH field were computed first on the orthonormal subdomain grid using smooth noise-robust differentiator kernels (discussed in Arbic, Scott, Chelton, Richman, and Shriver (2012)) before being merged using the above algorithm to avoid the appearance of high-frequency numerical artifacts (Martin et al., 2023) (a similar result can be obtained by a simple low-pass filtering of the mapped SSH).

### 1.6. Regional fine-tuning experiment

In S.I. Table 2 we show that NeurOST SSH-SST trained on global observations can be fine-tuned for regional applications to bring its performance closer to that of state-of-the-art regional schemes (Febvre et al., 2024; Martin et al., 2023). The global model was trained on 1 million training examples drawn randomly from the Global Ocean. During fine-tuning we started training from the converged global model using the Adam optimizer with a fixed learning rate parameter of $10^{-4}$ on a smaller training set of 100,000 examples drawn randomly from the Gulf Stream (as in our previous study (Martin et al., 2023)) and continued training until the validation loss stopped improving. This fine-tuning took 12 hours on a single node with four Nvidia V100 GPUs. The results presented in the rest of the study use only the global trained model to limit the computational resources of the method, but in future an ensemble of bespoke regional models could be fine-tuned to further optimize the SSH mapping in each region if these maps were produced operationally by a data centre. Since previous studies used a different test year, 2017, in the Gulf Stream (Ballarotta et al., 2021), we swapped 2017 and 2019 in our training-validation-testing split (S.I. Figure 2) to ensure 2017 was withheld during training and cross-validation (both the global and regional training were done with this updated split).

### 1.7. SSH map evaluation and inter-comparison OSE

To evaluate the accuracy and resolution of the SSH signals resolved by different mapping methods, we employ an 'observing system experiment' (OSE) in which each method is used to generate global gridded SSH estimates using all but one of the available satellite

altimeters which is then used as an independent validation of the mapped signal. Since the existing operational SSH products are only distributed using all available altimeters, performing an OSE would typically involve re-implementation of all existing methods, which would be challenging in the case of SSH mapping since the covariance parameters used to create the community-standard DUACS product are not publicly-available. To address this, in recent years a series of 'Ocean Data Challenges' have been developed (Metref et al., 2023). In each challenge a common mapping OSE problem is defined, developers of different methods implement their method and post their results, allowing a transparent performance benchmark.

To evaluate our global product, we use the recently-created global OSE challenge: '2023a_SSH_mapping_OSE' (Metref & Ballarotta, 2023). In this challenge, each method is used to create 1 year (2019) of global gridded SSH estimates using SSH observations from the satellites Jason 3, Sentinel 3A, Sentinel 3B, Haiyang-2A, Haiyang-2B, and Cryosat-2, while observations from the satellite Saral/Altika are withheld for validation. While the validation observations only sample the maps along 1D tracks, aggregating over a full year allows robust, geographically-varying error statistics to be found.

We present three SSH error metrics using the withheld altimeter, each averaged over the full year and binned into 1° bins: the root-mean-square error (RMSE) between the mapped and observed signals, the RMSE after applying a 70-250km along-track band-pass spatial filter to both the observed and mapped signals along the satellite tracks to highlight the maps' ability to map small mesoscale eddies, and the effective spatial resolution of the mapped signal. The effective resolution is found by taking along-track

segments of the withheld altimeter observations along with the mapped values at these locations and calculating the signal-to-noise ratio as a function of wavelength by dividing the power spectral density of the mapping errors by that of the observations. Concretely, the 'effective spatial resolution' is taken to be the wavelength at which the signal-to-noise ratio between the observed and mapped signals drops below 0.5 (Ballarotta et al., 2019).

To evaluate the surface currents inferred from each SSH map, surface drifter observations from the CMEMS global in-situ water velocity product (E.U. Copernicus Marine Service Information (CMEMS), 2024c) are used. Surface drifter observations are not used in the generation of any of the surface current maps presented here, so they are an independent validation dataset. We present geographically averaged velocity RMSE values for each method.

At the time of writing, three other SSH mapping methods have been implemented worldwide and all are available in the data challenge for evaluation: DUACS (Le Traon et al., 1998; Taburet et al., 2019), MIOST (geostrophic) (Ubelmann et al., 2021), and MIOST (geostrophic + equatorial waves) (Ballarotta et al., 2023). DUACS is the community-standard gridded SSH product that is distributed operationally by CMEMS. The DUACS system uses a linear optimal interpolation (OI) formulation (Bretherton et al., 1976), in which an *a priori* model is prescribed for how SSH covaries in space and in time, then the missing values are estimated using the best linear least-squares estimator. The assumed covariance, $C$, is

$$C\left(r,t\right)=\left(1+ar+\frac{1}{6}\left(ar\right)^{2}-\frac{1}{6}\left(ar\right)^{3}\right)\exp\left(-ar\right)\exp\left(\frac{-t^{2}}{T^{2}}\right), \tag{5}$$

where $t$ is the temporal separation of the observation and mapped point under consideration, $T$ is a prescribed de-correlation time-scale, $a = 3.337$, and

$$r = \sqrt{\left(\frac{dx - C_{px}t}{L_x}\right)^2 + \left(\frac{dy - C_{py}t}{L_y}\right)^2}, \tag{6}$$

where $L_x$ and $L_y$ are prescribed de-correlation length-scales in the zonal and meridional directions, $dx$ and $dy$ are respectively the zonal and meridional separation of the observation and mapped point under consideration, and $C_{px}$ and $C_{py}$ are prescribed propagation velocities. The de-correlation scales and propagation velocities are allowed to vary with geographical location and the values used are not publicly available but have been tuned over many years to best map mesoscale ocean features globally. The MIOST mapping method extends the linear mapping framework, using a wavelet decomposition to allow the construction of multiple independent components of the assumed covariance model (Ubelmann et al., 2022; Ballarotta et al., 2023). MIOST (geostrophic) uses a single component in the covariance model intended to represent the geostrophically balanced component of SSH evolution, while MIOST (geostrophy + equatorial waves) adds an additional component to model the propagation of tropical instability waves and Poincare waves near the equator.

### 1.8. Season definitions

Wherever results are split by season in this study we define those seasons in the Northern (Southern) Hemisphere: winter is January-March (July-September), spring is April-June (October-December), summer is July-September (January-March), and autumn is October-December (April-June).

### 1.9. Eddy kinetic energy

The kinetic energy, KE, per unit volume of the surface currents is calculated from the surface geostrophic current maps

$$\mathrm{KE} = \frac{\rho_0}{2}\left(u_g^2 + v_g^2\right), \tag{7}$$

where $\rho_0$ is a reference density taken to be 1025 kg m$^{-3}$. The eddy kinetic energy, EKE, is defined as the time-varying component of the KE

$$\mathrm{EKE} = \mathrm{KE} - \overline{\mathrm{KE}}, \tag{8}$$

where $\overline{\mathrm{KE}}$ is the time mean of the KE.

To highlight the difference in small-scale EKE between the maps we also calculate the EKE of the surface currents after the application of a 250km high-pass filter.

### 1.10. Relative vorticity, strain rate, and Okubo-Weiss quantity

While first order spatial derivatives of SSH give the velocity of the geostrophic currents, second order spatial derivatives quantify the deformation and rotation induced by the flow. The relative vorticity, $\omega$, describes the local rotation of the fluid (that is, how a patch of tracers would tend to rotate if placed at a point within the flow)

$$\omega = \frac{\partial v_g}{\partial x} - \frac{\partial u_g}{\partial y} = \frac{g}{f}\nabla_h^2\eta, \tag{9}$$

where $\nabla_h^2$ is the horizontal Laplacian.

Meanwhile, the strain rate, $s$, defines the deformation of fluid elements by the flow (that is, how a patch of tracers would change shape due to the flow)

$$s = \sqrt{s_n^2 + s_s^2} \tag{10}$$

where $s_n$ is the normal component of the strain

$$s_n = \frac{\partial u_g}{\partial x} - \frac{\partial v_g}{\partial y} = -2\frac{g}{f}\frac{\partial^2 \eta}{\partial x \partial y}, \tag{11}$$

and $s_s$ is the shear component

$$s_s = \frac{\partial v_g}{\partial x} + \frac{\partial u_g}{\partial y} = \frac{g}{f}\left(\frac{\partial^2 \eta}{\partial x^2} - \frac{\partial^2 \eta}{\partial y^2}\right). \tag{12}$$

A high strain rate is associated with the stretching of patches of fluid, is common in the areas between eddies, and is associated with the generation of submesoscale filaments through frontogenesis (Hoskins, 1982) and strong transfer of kinetic energy between scales (Aluie et al., 2018). Whereas strong relative vorticity (either positive or negative) is associated with coherent, persistent eddies and is typical in the cores of eddies.

The relative importance of relative vorticity and strain rate at each point in the fluid can be described using the Okubo-Weiss quantity (Okubo, 1970; Weiss, 1991),

$$W = s^2 - \omega^2, \tag{13}$$

which is positive when strain dominates and negative when relative vorticity dominates (Figure 3 in main text).

Note, DUACS vorticity/strain fields appear 'grainy' in comparison to NeurOST (e.g. in Fig. 3) due to DUACS having a coarser grid resolution. One could first linearly interpolate the DUACS data to a higher resolution grid before estimating vorticity and strain to reduce this, but we have verified that this has negligible impact on the accuracy and spectral characteristics of the vorticity (Fig. S11).

### 1.11. Eddy Dynamics Evaluation OSSE

As described in the main text, we use the GLORYS reanalysis product to implement an OSSE to evaluate the realism of eddy dynamics by generating synthetic altimetry observations from the reanalysis and inputting them to NeurOST. To ensure consistency with our OSE, we use 2019 as the test year and sample the GLORYS SSH along the locations of the 2019 altimeter tracks, applying regionally-varying white noise consistent with that described in the user guide for the along-track SSH observations (E.U. Copernicus Marine Service Information (CMEMS), 2024b, 2024a).

The metrics we use to evaluate the realism of the mapped surface currents and vorticity normalized skill scores that give the fraction of variance explained.

For surface currents this skill is defined as

$$\text{skill} = 1 - \frac{\text{MSE}\left(u_g\right) + \text{MSE}\left(v_g\right)}{\text{Var}\left(u_g\right) + \text{Var}\left(v_g\right)}, \tag{14}$$

where MSE is mean squared error and Var is the variance. Similarly for relative vorticity, $\zeta_g$, this is defined as

$$\text{skill} = 1 - \frac{\text{MSE}\left(\zeta_g\right)}{\text{Var}\left(\zeta_g\right)}. \tag{15}$$

### 1.12. KE cascade: diagnosing energy transfer between scales

Energy transfers between flows of different length-scales, a characteristic property of turbulent flows, can be diagnosed using a coarse-graining analysis (Aluie et al., 2018). By applying convolutions to the Navier-Stokes equation and neglecting small contributions from molecular viscosity, a kinetic energy (KE) budget for the coarse-grained flow (i.e. the velocity after convolution with a smoothing filter) is obtained (Aluie et al., 2018)

$$\frac{\partial}{\partial t}\rho_0\frac{|\overline{\mathbf{u}}_l|^2}{2} = -\nabla\cdot\mathbf{J}_l^{\text{transport}} - \Pi_l + \overline{\rho}_l\mathbf{g}\cdot\overline{\mathbf{u}}_l + \rho_0\overline{\mathbf{F}}_l^{\text{forcing}}\cdot\overline{\mathbf{u}}_l, \tag{16}$$

where $\bar{\cdot}_l$ represents convolution with a filter with scale diameter $l$, $\mathbf{J}_l^{\text{transport}}$ is the spatial transport of large-scale KE (as defined in Aluie et al. (2018)), $\rho_0$ is a reference density (here taken to be 1025kgm$^{-3}$), $\Pi_l$ is the transfer of energy between scales by non-linear eddy interactions defined below, $\mathbf{g}$ is the acceleration due to gravity, and $\overline{\mathbf{F}}_l^{\text{forcing}}$ is any external forcing at scales above $l$ (e.g. by winds). The third term on the right represents the conversion of potential energy into kinetic energy.

The existence of an upscale (or 'inverse') cascade of KE is a characteristic property of geophysical turbulence (Vallis, 2017) that is hypothesized to play a role in setting the seasonality of mesoscale ocean eddies (Sasaki et al., 2014; Qiu et al., 2014). We therefore here diagnose the transfer of KE between scales, $\Pi_l$, from surface geostrophic current maps to assess its magnitude and sign at different spatial scales, implicitly neglecting energy associated with vertical velocities (which are small at the scales considered here). We don't seek to close the energy budget in Equation 16 as this would require precise determination of the potential energy conversion and external forcing at the same resolution as the surface geostrophic current maps.

The KE cascade, $\Pi_l$, is caused by non-linear interactions between eddies and is characterized by the interplay between the large-scale strain tensor, $\overline{\mathbf{S}}_l$, and the subfilter-scale stress, $\overline{\tau}_l$, through (Aluie et al., 2018)

$$\Pi_l = -\rho_0 \overline{S}_{ij} \overline{\tau}_{ji}, \tag{17}$$

where

$$\overline{S}_{ij} = \frac{1}{2} \left( \partial_i \overline{u}_j + \partial_j \overline{u}_i \right), \tag{18}$$

$$\overline{\tau}_{ij} = \overline{u_i u_j} - \overline{u}_i \overline{u}_j, \tag{19}$$

repeated indices are summed over, and the subscript $l$ in the coarse-graining operation has been dropped when using index notation to avoid confusion between the coarse-graining length scale and a spatial index. The cascade term, $\Pi_l$, represents the energy transfer from scales larger than $l$ to smaller scales due to non-linear eddy interactions, so $\Pi_l$ is positive (negative), energy is transferred from scales larger (smaller) than $l$ to smaller (larger) scales representing a downscale (upscale) cascade. Scrutiny of Equation 17 highlights the sensitivity of the KE cascade to the strain rate, and hence to eddy geometry.

We use an open-source code, FlowSieve (Storer & Aluie, 2023), to coarse-grain the surface geostrophic current maps at a range of scales, $l$, and diagnose $\Pi_l$ and $\mathbf{J}_l^{\text{transport}}$. While this coarse-graining can be done on global surface current fields accounting for the spherical geometry of the Earth's surface (Storer & Aluie, 2023), we here restrict our attention to a selection of open ocean regions (defined in S.I. Table 2). This prevents the need to prescribe boundary conditions at coastlines and significantly reduces the computational requirements of the analysis. All velocities are first projected onto a local ortho-normal grid with a grid spacing 10km and side length of 2560km. We perform coarse-graining on this grid and diagnose $\Pi_l$ and $\mathbf{J}_l^{\text{transport}}$ as a function of $l$ and time at each grid point, before taking a spatial average of both quantities over a smaller box in the centre of the domain with side length 1280km. The smoothing filter used in the coarse-graining is a smoothed top-hat, as used in previous studies (Storer et al., 2022)

$$G_l(\mathbf{r}) = \frac{A}{2}\left(1 - \tanh\left[10\left(\frac{|\mathbf{r}|}{l/2} - 1\right)\right]\right), \tag{20}$$

where $A$ is a normalization calculated numerically to ensure $G_l$ integrates to unity and $\mathbf{r}$ is the separation between the evaluation point and the center of the convolutional kernel.

The coarse-grained fields, $\overline{f}_l(\mathbf{x})$, are then defined as

$$\overline{f}_l(\mathbf{x}) = G_l * f, \tag{21}$$

where $*$ is a two-dimensional convolution.

There is no direct correspondence between the filter scales, $l$, used in coarse-graining and wavelengths in a Fourier analysis (e.g. the KE spectra in Figure 5 in the Main Text). To aid interpretation of the coarse-graining results in comparison to the spectral analysis we used to evaluate the effective resolution of each SSH map, we empirically calculate associated effective coarse-graining scales for each SSH map (method described below).

When assessing the ability of the KE cascade to drive the summer-time peak in large-scale KE, we compare the change in large-scale KE from its winter minimum to its summer maximum to the time integrals of $(-\Pi_l)$ and $(-\nabla \cdot \mathbf{J}_l^{\text{transport}})$ over the same time period. This analysis neglects sources/sinks of energy at larger scales, energy lost from surface currents due to eddy barotropization, and conversion of potential energy to KE but in this study we don't seek to close the large-scale KE budget, merely to demonstrate that the diagnosed $\Pi_l$ is greatly changed between maps and that its strength becomes large enough to be a significant contributor to the change in large-scale KE.

During testing we also tried estimating KE cascades using the Fourier method used in Scott and Wang (2005) but found negligible differences to the results obtained using coarse-graining.

### 1.13. KE Wavenumber Spectrum Calculation

To calculate the KE wavenumber spectra in Figure 5 of the main text we calculated 2D KE wave-number spectra on a local, ortho-normal grid and azimuthally averaged to collapse the meridional and zonal dimensions into a single wavenumber.

## 2. Text S2: Effective coarse-graining scale of SSH maps

To aid interpretation of the effective resolution metric (Ballarotta et al., 2019), we also provide a corresponding 'effective coarse-graining scale'. This metric can be interpreted as the coarse-graining scale that best represents the smoothing induced by the SSH mapping algorithm and is useful when considering our KE cascade results which were obtained using coarse-graining.

The effective coarse-graining scale is obtained by positing that the mapped signal can reasonably be approximated as a coarsened version of the true signal where a smoothing kernel has been convolved with the observations.

For a mapped along-track signal x, and an observed signal y, the effective resolution is defined (Ballarotta et al., 2019) as the wavelength where the function, $f$, crosses 0.5, where

$$f(k) = 1 - \frac{\widehat{(x-y)}^{*}\widehat{(x-y)}}{\hat{y}^{*}\hat{y}}, \tag{22}$$

where $^{*}$ represents complex conjugation, a "hat" is the Fourier transform, and $k$ is the along-track wavenumber.

We suppose that the mapped signal, $x$, can be approximated as the convolution of $y$ with a smoothing kernel, $G_l$, with corresponding spatial scale, $l$,

$$x = G_l * y. \tag{23}$$

Using the convolution theorem and plugging this definition of $x$ into Equation 22 yields an expression for $f$ in terms of the smoothing kernel

$$f(k) = \hat{G}_l + \hat{G}_l^{\,*} - \hat{G}_l^{\,*}\hat{G}_l. \tag{24}$$

For any given kernel, $G_l$, its Fourier transform, and hence $f(k)$, depends only on the coarse-graining scale, $l$. Thus for each map and region we fit the function in Equation 24 to the data for $f(k)$ for different coarse-graining kernels, $G_l$, to find corresponding coarse-graining scales, $l$. We refer to the resulting scale as the 'effective coarse-graining scale' of the SSH map for each kernel.

In S.I. Table 2, we compare the effective resolution to the effective coarse-graining scales for a Gaussian kernel

$$G_l^{\text{Gaussian}}(x - x') = \frac{1}{l\sqrt{2\pi}} \exp\left(-\frac{|x - x'|^2}{2l^2}\right), \tag{25}$$

and the smooth top-hat kernel

$$G_l^{\text{FlowSieve}}(x - x') = \frac{A}{2}\left(1 - \tanh\left[10\left(\frac{|x - x'|}{l/2} - 1\right)\right]\right), \tag{26}$$

used in FlowSieve (Storer & Aluie, 2023) that we used to diagnose the energy transfer between scales, where $|x - x'|$ is the distance between the analysis point and the kernel center and $A$ is a normalization factor computed numerically. Note that for $G_l^{\text{FlowSieve}}$ the Fourier transform becomes oscillatory at high wavenumbers, we therefore set all values of the fitted $f(k)$ to zero at wavenumbers past the first zero crossing to ensure we only fit the physically meaningful part of the curve to the data.

**Movie S1.** Movie of relative vorticity in the Subtropical North Pacific (150-160°W, 20-30°N) from NeurOST SSH-SST, DUACS, and GLORYS.

**Movie S2.** Movie of relative vorticity in the Subtropical North Pacific (150-160°W, 20-30°N) from the NeurOST reconstruction of GLORYS and from GLORYS.

## References

Aluie, H., Hecht, M., & Vallis, G. K. (2018). Mapping the energy cascade in the North Atlantic Ocean: The coarse-graining approach. *Journal of Physical Oceanography*, *48*(2), 225–244.

Arbic, B. K., Scott, R. B., Chelton, D. B., Richman, J. G., & Shriver, J. F. (2012). Effects of stencil width on surface ocean geostrophic velocity and vorticity estimation from gridded satellite altimeter data. *Journal of Geophysical Research: Oceans*, *117*(C3).

Archambault, T., Filoche, A., Charantonis, A., Béréziat, D., & Thiria, S. (2024). Learning sea surface height interpolation from multi-variate simulated satellite observations. *Journal of Advances in Modeling Earth Systems*, *16*(6), e2023MS004047.

Ballarotta, M., Metref, S., Albery, A., Cosme, E., Beauchamp, M., & Le Guillou, F. (2021). *Ocean data challenges.* (`https://github.com/ocean-data-challenges/2021a_SSH_mapping_OSE`)

Ballarotta, M., Ubelmann, C., Pujol, M.-I., Taburet, G., Fournier, F., Legeais, J.-F., ... others (2019). On the resolutions of ocean altimetry maps. *Ocean Science*, *15*(4), 1091–1109.

Ballarotta, M., Ubelmann, C., Veillard, P., Prandi, P., Etienne, H., Mulet, S., ... Picot, N. (2023). Improved global sea surface height and current maps from remote sensing and in situ observations. *Earth System Science Data*, *15*(1), 295–315.

Bretherton, F. P., Davis, R. E., & Fandry, C. (1976). A technique for objective analysis

and design of oceanographic experiments applied to MODE-73. In *Deep sea research and oceanographic abstracts* (Vol. 23, pp. 559–582).

Callaham, J. L., Maeda, K., & Brunton, S. L. (2019). Robust flow reconstruction from limited measurements via sparse representation. *Physical Review Fluids*, *4*(10), 103907.

Cao, Y., Dong, C., Stegner, A., Bethel, B. J., Li, C., Dong, J., ... Yang, J. (2023). Global sea surface cyclogeostrophic currents derived from satellite altimetry data. *Journal of Geophysical Research: Oceans*, *128*(1), e2022JC019357.

Chin, T. M., Vazquez-Cuervo, J., & Armstrong, E. M. (2017). A multi-scale high-resolution analysis of global sea surface temperature. *Remote sensing of environment*, *200*, 154–169.

E.U. Copernicus Marine Service Information (CMEMS). (2024a). *Global ocean along track l 3 sea surface heights NRT.* Retrieved from `https://doi.org/10.48670/moi-00147` (Accessed on 07-04-2024)

E.U. Copernicus Marine Service Information (CMEMS). (2024b). *Global ocean along track l 3 sea surface heights reprocessed 1993 ongoing tailored for data assimilation.* Retrieved from `https://doi.org/10.48670/moi-00146` (Accessed on 07-04-2024)

E.U. Copernicus Marine Service Information (CMEMS). (2024c). *Global ocean-delayed mode in situ observations of surface (drifters, HFR) and sub-surface (vessel-mounted adcps) water velocity.* Retrieved from `https://doi.org/10.17882/86236` (Accessed on 07-04-2024)

Fablet, R., Amar, M. M., Febvre, Q., Beauchamp, M., & Chapron, B. (2021). End-

to-end physics-informed representation learning for satellite ocean remote sensing data: Applications to satellite altimetry and sea surface currents. *ISPRS Annals of Photogrammetry, Remote Sensing & Spatial Information Sciences*(3).

Febvre, Q., Le Sommer, J., Ubelmann, C., & Fablet, R. (2024). Training neural mapping schemes for satellite altimetry with simulation data. *Journal of Advances in Modeling Earth Systems*, *16*(7), e2023MS003959. Retrieved from `https://agupubs.onlinelibrary.wiley.com/doi/abs/10.1029/2023MS003959` doi: https://doi.org/10.1029/2023MS003959

Gao, Z., Tan, C., Wu, L., & Li, S. Z. (2022, June). SimVP: Simpler yet better video prediction. In *Proceedings of the ieee/cvf conference on computer vision and pattern recognition (cvpr)* (p. 3170-3180).

Hoskins, B. J. (1982). The mathematical theory of frontogenesis. *Annual Review of Fluid Mechanics*, *14*(1), 131–151.

JPL MUR MEaSUREs Project. (2015). *GHRSST level 4 MUR global foundation sea surface temperature analysis. ver. 4.1.* Retrieved from `https://doi.org/10.5067/GHGMR-4FJ04` (Accessed on 07-04-2024)

Lagerloef, G. S., Mitchum, G. T., Lukas, R. B., & Niiler, P. P. (1999). Tropical Pacific near-surface currents estimated from altimeter, wind, and drifter data. *Journal of Geophysical Research: Oceans*, *104*(C10), 23313–23326.

Le Traon, P., Nadal, F., & Ducet, N. (1998). An improved mapping method of multisatellite altimeter data. *Journal of Atmospheric and Oceanic Technology*, *15*(2), 522–534.

Manucharyan, G. E., Siegelman, L., & Klein, P. (2021). A deep learning approach to spatiotemporal sea surface height interpolation and estimation of deep currents in geostrophic ocean turbulence. *Journal of Advances in Modeling Earth Systems*, *13*(1), e2019MS001965.

Martin, S. A., Manucharyan, G. E., & Klein, P. (2023). Synthesizing sea surface temperature and satellite altimetry observations using deep learning improves the accuracy and resolution of gridded sea surface height anomalies. *Journal of Advances in Modeling Earth Systems*, *15*(5), e2022MS003589.

Metref, S., & Ballarotta, M. (2023). *Ocean data challenges.* (`https://github.com/ocean-data-challenges/2023a_SSH_mapping_OSE`)

Metref, S., Ballarotta, M., Le Sommer, J., Cosme, E., Albert, A., Beauchamp, M., ... Febvre, Q. (2023). *Ocean data challenges.* (`https://ocean-data-challenges.github.io/`)

Okubo, A. (1970). Horizontal dispersion of floatable particles in the vicinity of velocity singularities such as convergences. In *Deep sea research and oceanographic abstracts* (Vol. 17, pp. 445–454).

Penven, P., Halo, I., Pous, S., & Marié, L. (2014). Cyclogeostrophic balance in the Mozambique Channel. *Journal of Geophysical Research: Oceans*, *119*(2), 1054–1067.

Qiu, B., Chen, S., Klein, P., Sasaki, H., & Sasai, Y. (2014). Seasonal mesoscale and submesoscale eddy variability along the north pacific subtropical countercurrent. *Journal of Physical Oceanography*, *44*(12), 3079–3098.

Rio, M.-H., Mulet, S., & Picot, N. (2014). Beyond GOCE for the ocean circulation

estimate: Synergetic use of altimetry, gravimetry, and in situ data provides new insight into geostrophic and ekman currents. *Geophysical Research Letters*, *41*(24), 8918–8925.

Sasaki, H., Klein, P., Qiu, B., & Sasai, Y. (2014). Impact of oceanic-scale interactions on the seasonal modulation of ocean dynamics by the atmosphere. *Nature Communications*, *5*(1), 5636.

Scott, R. B., & Wang, F. (2005). Direct evidence of an oceanic inverse kinetic energy cascade from satellite altimetry. *Journal of Physical Oceanography*, *35*(9), 1650–1666.

Shi, X., Chen, Z., Wang, H., Yeung, D.-Y., Wong, W.-K., & Woo, W.-c. (2015). Convolutional LSTM network: A machine learning approach for precipitation nowcasting. *Advances in neural information processing systems*, *28*.

Srivastava, N., Mansimov, E., & Salakhudinov, R. (2015). Unsupervised learning of video representations using LSTMs. In *International conference on machine learning* (pp. 843–852).

Storer, B. A., & Aluie, H. (2023). FlowSieve: A coarse-graining utility for geophysical flows on the sphere. *Journal of Open Source Software*, *8*(84), 4277.

Storer, B. A., Buzzicotti, M., Khatri, H., Griffies, S. M., & Aluie, H. (2022). Global energy spectrum of the general oceanic circulation. *Nature Communications*, *13*(1), 5314.

Taburet, G., Sanchez-Roman, A., Ballarotta, M., Pujol, M.-I., Legeais, J.-F., Fournier, F., ... Dibarboure, G. (2019). DUACS DT2018: 25 years of reprocessed sea level

altimetry products. *Ocean Science*, *15*(5), 1207–1224.

Tan, C., Gao, Z., Li, S., & Li, S. Z. (2022). SimVP: Towards simple yet powerful spatiotemporal predictive learning. *arXiv preprint arXiv:2211.12509*.

Ubelmann, C., Carrere, L., Durand, C., Dibarboure, G., Faugère, Y., Ballarotta, M., ... Lyard, F. (2022). Simultaneous estimation of ocean mesoscale and coherent internal tide sea surface height signatures from the global altimetry record. *Ocean Science*, *18*(2), 469–481.

Ubelmann, C., Dibarboure, G., Gaultier, L., Ponte, A., Ardhuin, F., Ballarotta, M., & Faugère, Y. (2021). Reconstructing ocean surface current combining altimetry and future spaceborne Doppler data. *Journal of Geophysical Research: Oceans*, *126*(3), e2020JC016560.

Vallis, G. K. (2017). *Atmospheric and oceanic fluid dynamics*. Cambridge University Press.

Weiss, J. (1991). The dynamics of enstrophy transfer in two-dimensional hydrodynamics. *Physica D: Nonlinear Phenomena*, *48*(2-3), 273–294.

| Region | Mapping Method | RMSE [cm] | RMSE (70-250km) [cm] | Eff. Res. [km] |
|---|---|---|---|---|
| Gulf Stream (295-305°E, 33-43°N) | DUACS | 5.66 | 2.44 | 126 |
| | MIOST (geos) | 5.61 | 2.41 | 120 |
| | NeurOST SSH | 5.33 | 2.29 | 114 |
| | NeurOST SSH-SST | **5.01** | **2.19** | **107** |
| | GLORYS | 12.47 | 5.25 | 236.5 |
| N Atlantic (322-338°E, 39-51°N) | DUACS | 4.15 | 1.33 | 133 |
| | MIOST (geos + waves) | 3.86 | 1.25 | 129 |
| | NeurOST SSH | 3.85 | 1.19 | 121 |
| | NeurOST SSH-SST | **3.78** | **1.12** | **116** |
| | GLORYS | 6.45 | 2.31 | 201 |
| Mediterranean (2-19°E, 31-44°N) | DUACS | 4.24 | 1.02 | 150 |
| | MIOST (geos + waves) | 3.97 | 0.97 | 128 |
| | NeurOST SSH | 3.95 | 0.98 | 112 |
| | NeurOST SSH-SST | **3.90** | **0.94** | **112** |
| | GLORYS | 6.25 | 1.94 | 220 |
| Kuroshio (153-167°E, 29-41°N) | DUACS | 5.03 | 2.00 | 163 |
| | MIOST (geos + waves) | 4.68 | 1.80 | 150 |
| | NeurOST SSH | 4.52 | 1.69 | 138 |
| | NeurOST SSH-SST | **4.34** | **1.57** | **128** |
| | GLORYS | 8.50 | 3.14 | 219 |
| Subtropical N Pacific (149-161°E, 19-31°N) | DUACS | 3.79 | 1.47 | 197 |
| | MIOST (geos + waves) | 3.70 | 1.39 | 185 |
| | NeurOST SSH | 3.51 | 1.29 | 171 |
| | NeurOST SSH-SST | **3.42** | **1.22** | **156** |
| | GLORYS | 5.62 | 1.89 | 246 |
| Equatorial Pacific (175-250°E, 10°S-10°N) | DUACS | 3.30 | 1.11 | 490 |
| | MIOST (geos + waves) | 3.21 | 1.10 | **445** |
| | NeurOST SSH | 3.21 | 1.10 | 456 |
| | NeurOST SSH-SST | **3.19** | **1.09** | 448 |
| | GLORYS | 4.17 | 1.12 | 499 |
| Brazil-Malvinas (305-325°E, 40-55°S) | DUACS | 4.55 | 1.74 | 121 |
| | MIOST (geos) | 4.45 | 1.74 | 118 |
| | NeurOST SSH | 4.38 | 1.67 | 113 |
| | NeurOST SSH-SST | **4.09** | **1.47** | **103** |
| | GLORYS | 11.28 | 4.16 | 248 |
| Agulhas (10-30°E, 35-45°S) | DUACS | 6.09 | 2.55 | 144 |
| | MIOST (geos + waves) | 6.05 | 2.52 | 141 |
| | NeurOST SSH | 5.78 | 2.35 | 127 |
| | NeurOST SSH-SST | **5.54** | **2.19** | **118** |
| | GLORYS | 12.01 | 4.97 | 254 |
| Subtropical S Pacific (194-206°E, 19-31°S) | DUACS | 3.25 | 1.11 | 186 |
| | MIOST (geos + waves) | 3.10 | 1.06 | 174 |
| | NeurOST SSH | 3.05 | 0.99 | 162 |
| | NeurOST SSH-SST | **2.97** | **0.93** | **148** |
| | GLORYS | 4.87 | 1.40 | 224 |
| Drake Passage (290-300°E, 55-65°S) | DUACS | 4.49 | 1.60 | 115 |
| | MIOST (geos + waves) | 4.44 | 1.62 | 110 |
| | NeurOST SSH | 4.27 | 1.53 | 108 |
| | NeurOST SSH-SST | **4.14** | **1.44** | **97** |
| | GLORYS | 8.68 | 3.46 | 230 |

Table S1: RMSE, filtered RMSE (signals between 70-250km), and effective resolution of the existing global SSH products compared to our deep learning method with and without SST in a selection of regions (Metref & Ballarotta, 2023). We show only the variant of the MIOST method that gives the best RMSE in each region. Bold values indicate the best-performing method on each metric.

| Region | Mapping Method | RMSE [cm] | RMSE (70-250km) [cm] | Eff. Res. [km] |
|---|---|---|---|---|
| Gulf Stream | DUACS | 7.50 (5.66) | 3.48 (2.44) | 159 (126) |
| | NeurOST SSH-SST | **5.58** (5.01) | **2.39** (2.19) | **115** (107) |
| N Atlantic | DUACS | 4.64 (4.15) | 1.64 (1.33) | 153 (133) |
| | NeurOST SSH-SST | **3.92** (3.78) | **1.23** (1.12) | **122** (116) |
| Mediterranean | DUACS | 4.49 (4.24) | 1.27 (1.02) | 250 (150) |
| | NeurOST SSH-SST | **4.01** (3.90) | **1.06** (0.94) | **144** (112) |
| Kuroshio | DUACS | 6.16 (5.03) | 2.65 (2.00) | 197 (163) |
| | NeurOST SSH-SST | **4.65** (4.34) | **1.77** (1.57) | **139** (128) |
| Subtropical N Pacific | DUACS | 4.21 (3.79) | 1.74 (1.47) | 227 (197) |
| | NeurOST SSH-SST | **3.54** (3.42) | **1.31** (1.22) | **169** (156) |
| Equatorial Pacific | DUACS | 3.40 (3.30) | 1.14 (1.11) | 566 (490) |
| | NeurOST SSH-SST | **3.25** (3.19) | **1.10** (1.09) | **472** (448) |
| Brazil-Malvinas | DUACS | 5.98 (4.55) | 2.55 (1.74) | 152 (121) |
| | NeurOST SSH-SST | **4.50** (4.09) | **1.74** (1.47) | **110** (103) |
| Agulhas | DUACS | 7.85 (6.09) | 3.53 (2.55) | 176 (144) |
| | NeurOST SSH-SST | **6.05** (5.54) | **2.50** (2.19) | **128** (118) |
| Subtropical S Pacific | DUACS | 3.51 (3.25) | 1.27 (1.11) | 206 (186) |
| | NeurOST SSH-SST | **3.03** (2.97) | **0.97** (0.93) | **155** (148) |
| Drake Passage | DUACS | 4.98 (4.49) | 1.96 (1.60) | 131 (115) |
| | NeurOST SSH-SST | **4.31** (4.14) | **1.56** (1.44) | **108** (97) |

Table S2: Evaluation of DUACS and NeurOST SSH-SST maps generated using the stable constellation of 2 satellite altimeters operational since 1993 and used in climate studies. The metrics are as in Table S2. Bold values indicate the best performing method on each metric. Numbers in brackets give metrics for the 6 altimeter constellation (as in Table S2).

| Mapping Method | RMSE [cm] | Effective Resolution [km] |
|---|---|---|
| DUACS (Taburet et al., 2019) | 7.82 | 152 |
| MIOST (geos) (Ubelmann et al., 2021) | 6.93 | 140 |
| DYMOST (Ubelmann et al., 2015) | 6.75 | 129 |
| BFN-QG (Le Guillou et al., 2021) | 7.69 | 122 |
| 4DVarNet SSH (2022) (Beauchamp et al., 2022) | 6.63 | 110 |
| 4DVarNet SSH (2023) (Febvre et al., 2024) | **6.00** | **100** |
| MUSTI (Archambault et al., 2023) | 6.40 | 115 |
| ConvLSTM SSH (Martin et al., 2023) | 6.46 | 114 |
| ConvLSTM SSH-SST (Martin et al., 2023) | 6.00 | 100 |
| NeurOST SSH-SST (global) | 6.18 | 114 |
| NeurOST SSH-SST (fine-tuned) | 6.04 | 108 |

Table S3: RMSE and effective resolution of published SSH mapping methods in the Gulf Stream (Ballarotta et al., 2021). Bold values indicate the best-performing method on each metric. Note that the results for ConvLSTM shown here differ from those published in our previous work (Martin et al., 2023) as the maps used here were created by merging multiple patch reconstructions together (as described in Text S1), however, the network and weights used are the same as in our previous study.

| Region | Mapping Method | Eff. Res. [km] | Eff. Scale ($G_l^{\text{Gaussian}}$) [km] | Eff. Scale ($G_l^{\text{FlowSieve}}$) [km] |
|---|---|---|---|---|
| Gulf Stream | DUACS | 126 | 31.3 | 90.5 |
| | MIOST (geos) | 120 | 29.5 | 84.6 |
| | NeurOST SSH | 114 | 28.1 | 79.5 |
| | NeurOST SSH-SST | **107** | **26.5** | **76.7** |
| N Atlantic | DUACS | 133 | 33.4 | 95.7 |
| | MIOST (geos + waves) | 129 | 31.8 | 92.2 |
| | NeurOST SSH | 121 | 30.1 | 86.1 |
| | NeurOST SSH-SST | **116** | **28.5** | **83.0** |
| Mediterranean | DUACS | 150 | 32.7 | - |
| | MIOST (geos + waves) | 128 | **28.3** | - |
| | NeurOST SSH | 112 | 30.9 | - |
| | NeurOST SSH-SST | **112** | 30.9 | - |
| Kuroshio | DUACS | 163 | 40.1 | 115.7 |
| | MIOST (geos + waves) | 150 | 36.6 | 104.9 |
| | NeurOST SSH | 138 | 34.3 | 99.8 |
| | NeurOST SSH-SST | **128** | **31.8** | **92.4** |
| Subtropical N Pacific | DUACS | 197 | 45.9 | 132.3 |
| | MIOST (geos + waves) | 185 | 42.8 | 120.5 |
| | NeurOST SSH | 171 | 39.4 | 109.4 |
| | NeurOST SSH-SST | **156** | **36.1** | **103.8** |
| Equatorial Pacific | DUACS | 490 | 108.1 | - |
| | MIOST (geos + waves) | **445** | 104.2 | - |
| | NeurOST SSH | 456 | 103.3 | - |
| | NeurOST SSH-SST | 448 | **101.6** | - |
| Brazil-Malvinas | DUACS | 121 | 29.8 | 85.1 |
| | MIOST (geos) | 118 | 29.3 | 84.3 |
| | NeurOST SSH | 113 | 28.0 | 79.6 |
| | NeurOST SSH-SST | **103** | **25.7** | **73.5** |
| Agulhas | DUACS | 144 | 36.4 | 104.3 |
| | MIOST (geos + waves) | 141 | 35.0 | 102.3 |
| | NeurOST SSH | 127 | 31.4 | 91.7 |
| | NeurOST SSH-SST | **118** | **29.2** | **84.9** |
| Subtropical S Pacific | DUACS | 186 | 45.8 | 132.5 |
| | MIOST (geos + waves) | 174 | 42.7 | 120.7 |
| | NeurOST SSH | 162 | 39.2 | 109.7 |
| | NeurOST SSH-SST | **148** | **35.7** | **103.4** |
| Drake Passage | DUACS | 115 | 28.8 | 80.8 |
| | MIOST (geos + waves) | 110 | 27.5 | 78.0 |
| | NeurOST SSH | 108 | 27.2 | 77.7 |
| | NeurOST SSH-SST | **97** | **25.4** | **72.7** |

Table S4: Effective resolution and effective coarse-graining scales for both a standard Gaussian kernel, $G_l^{\text{Gaussian}}$, and the smooth top-hat kernel used in FlowSieve, $G_l^{\text{FlowSieve}}$, as defined in Methods. Bold values indicate best performing method on each metric. Effective coarse-graining scales for $G_l^{\text{FlowSieve}}$ are not given for the Mediterranean and the Equatorial Pacific since this kernel did not provide a good fit for the observed signal-to-noise ratio (Text S2) in these regions.

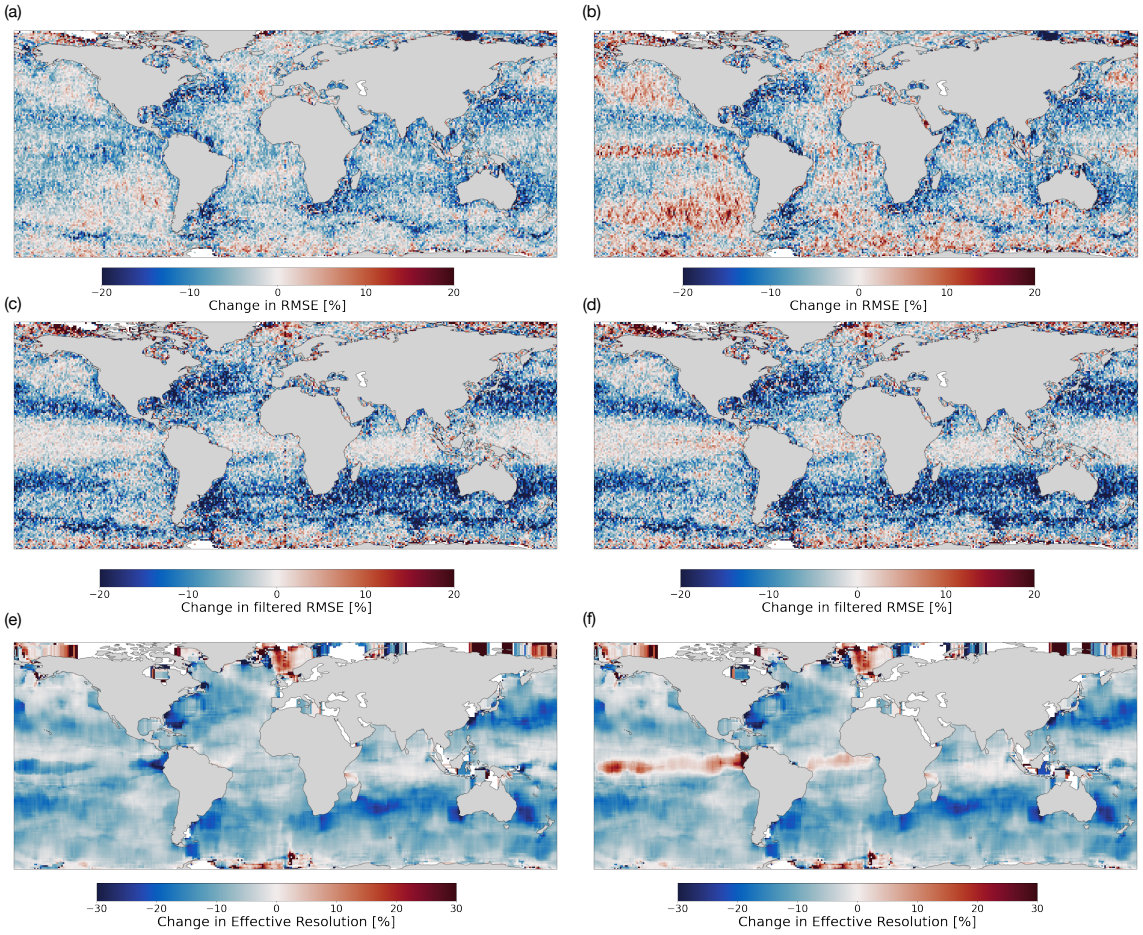


Figure S1: (a) Change in RMSE for NeurOST SSH-SST compared to MIOST (geos.) (b) Same as (a) but for NeurOST SSH-SST compared to MIOST (geos. + waves). (c) Change in RMSE for wavelengths between 70 and 250km for NeurOST SSH-SST compared to MIOST (geos.). (d) Same as (c) but for NeurOST SSH-SST compared to MIOST (geos. + waves). (e) Change in smallest resolved wavelength for NeurOST SSH-SST compared to MIOST (geos.). (f) Same as (e) but for NeurOST SSH-SST compared to MIOST (geos. + waves).

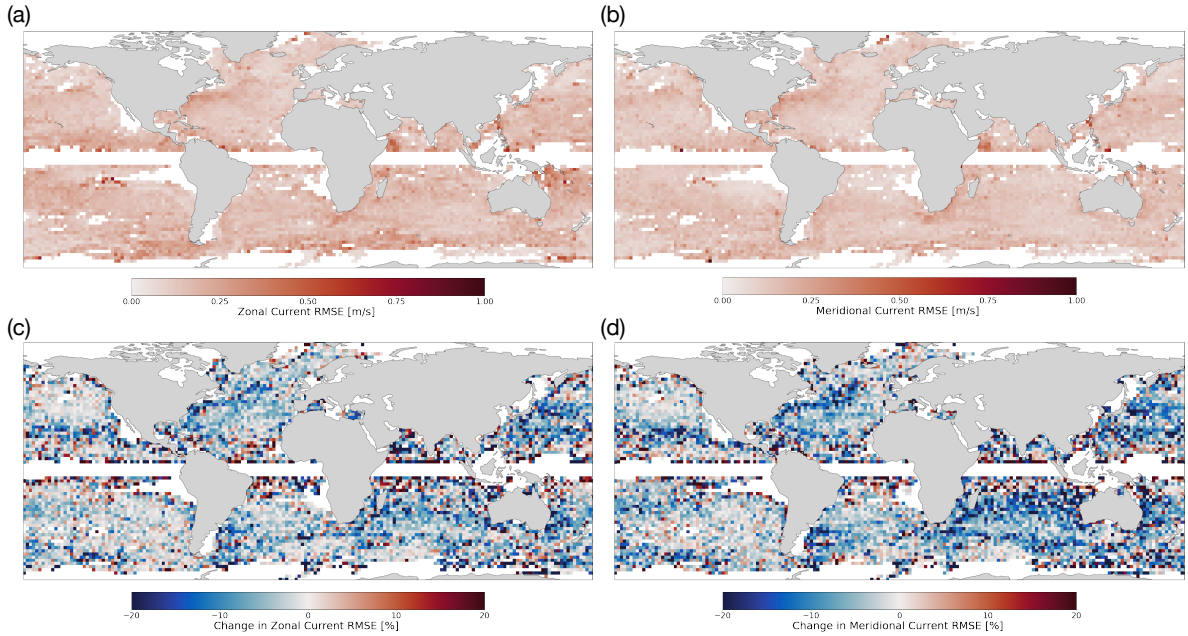


Figure S2: (a) RMSE of NeurOST SSH-SST zonal surface geostrophic currents compared to surface drifters. (b) Same as (a) but for the meridional currents. c, Change in zonal current RMSE for NeurOST SSH-SST compared to DUACS. (d) Same as (c) but for the meridional currents.

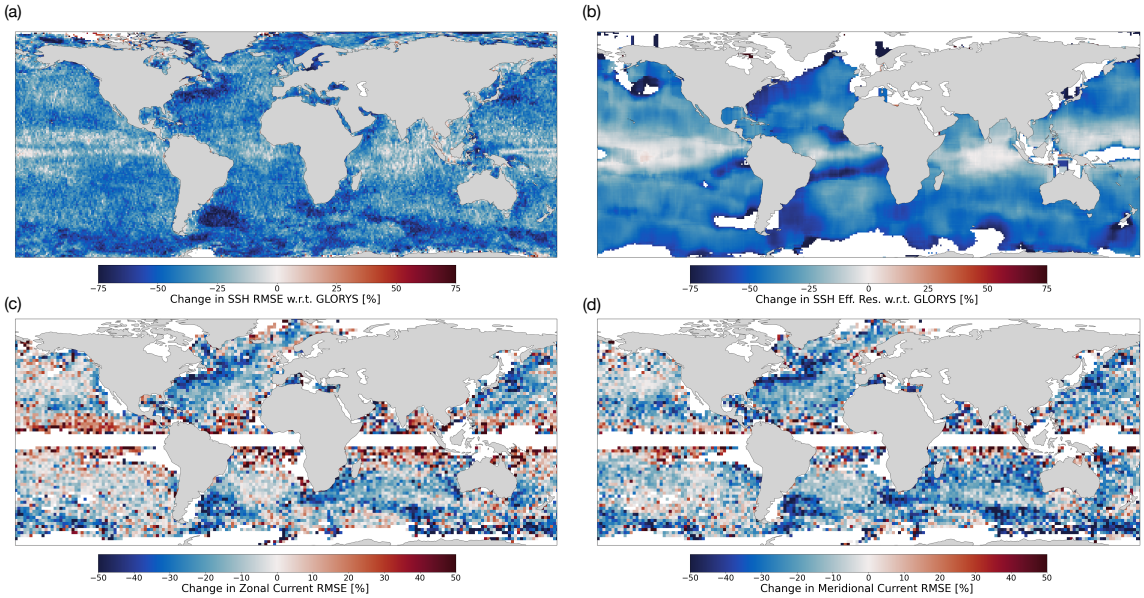


Figure S3: (a) Change in SSH RMSE for NeurOST SSH-SST compared to GLORYS. (b) Same as (a) but for effective spatial resolution. (c) Change in RMSE of zonal surface current for NeurOST SSH-SST compared to GLORYS. (d) Same as (c) but for meridional current.

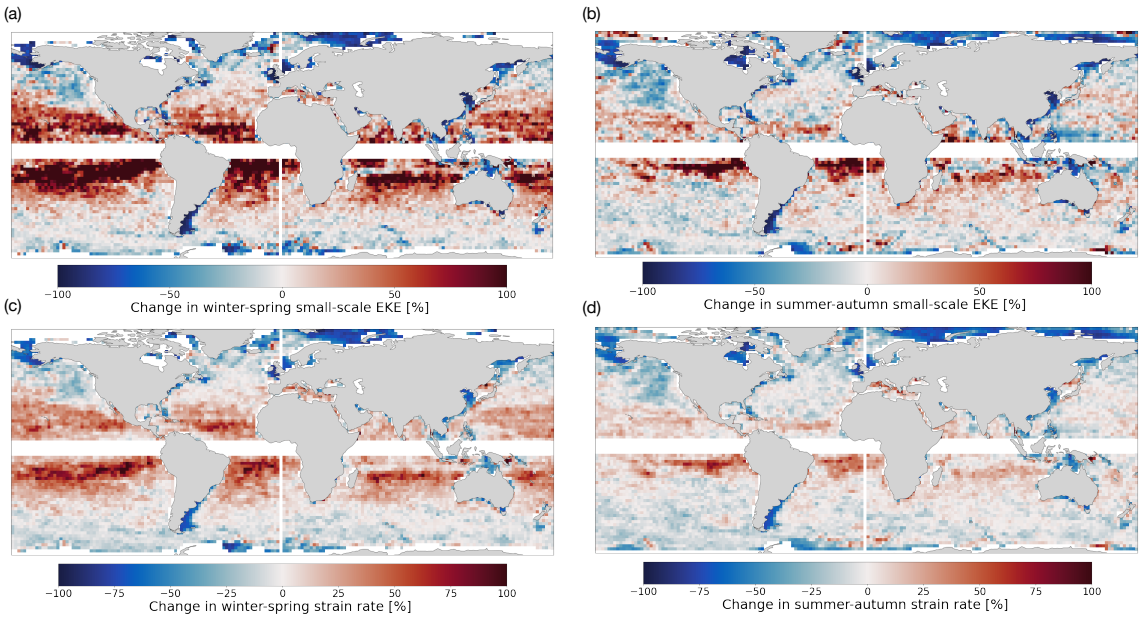


Figure S4: Changes in diagnostics of eddy energy and dynamics from NeurOST SSH-SST currents compared to DUACS. (a) Winter-spring mean EKE for flows with wavelength below 250km. (b) Same as (a) but averaged over summer and autumn. (c) Winter-spring mean strain rate. (d) same as (c) but averaged over summer and autumn. Absolute values of these quantities are shown in S.I. Figure S5.

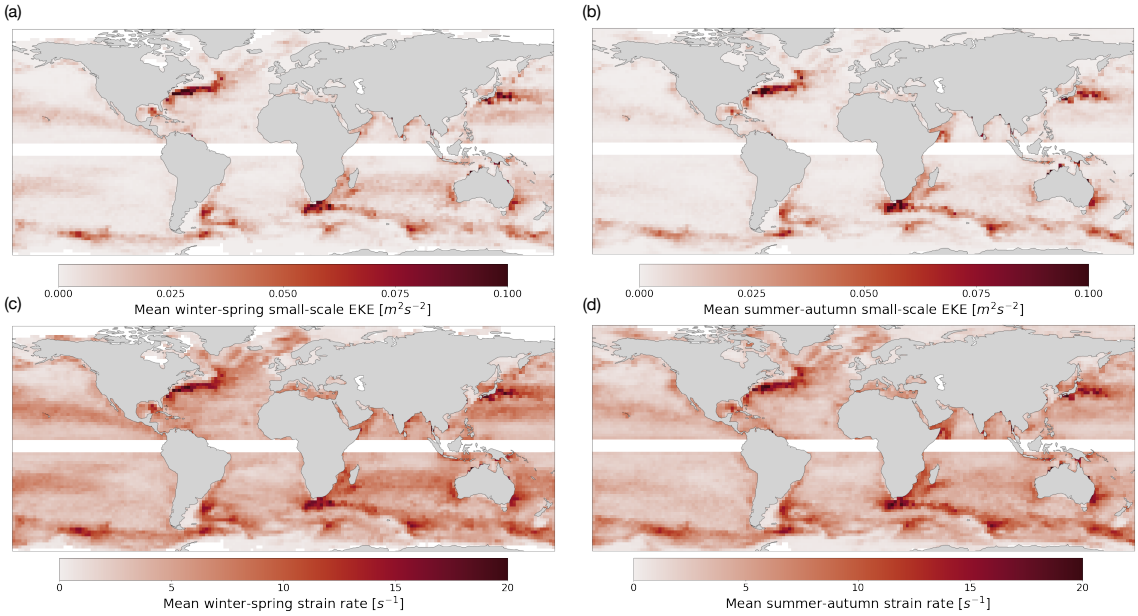


Figure S5: Absolute values of the fields in S.I. Figure S4 calculated from NeurOST SSH-SST maps.

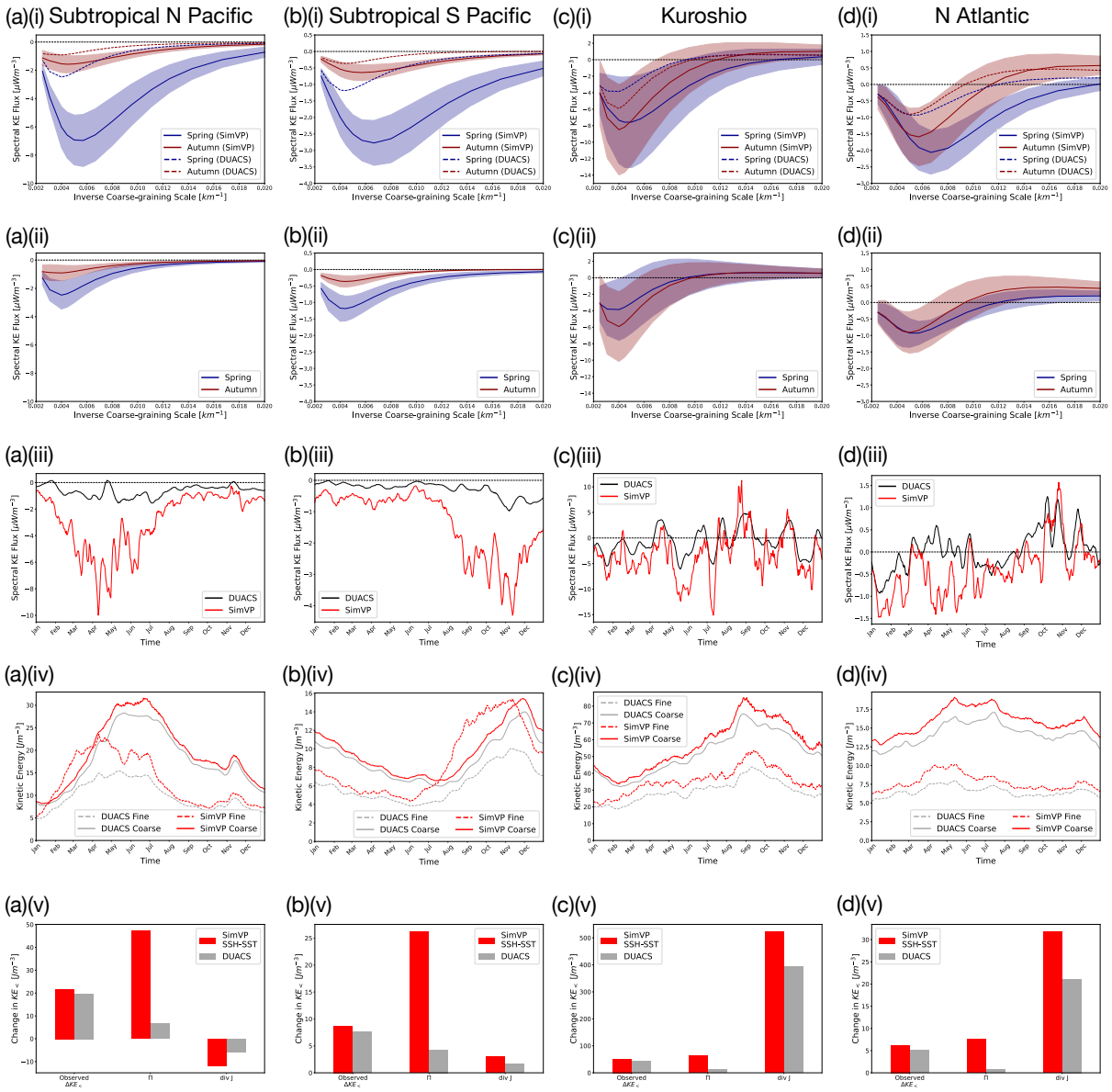


Figure S6: (a) Subtropical North Pacific (149-161E, 19-31N). (i) Mean (solid lines) and standard deviation (shading) of KE cascade from NeurOST SSH-SST surface currents for the seasons of maximum (Spring) and minimum (Autumn) upscale cascade with mean DUACS cascades for reference (dashed lines). (ii) Same as (i) but from DUACS. (iii) Time-series of KE cascade across 250km for both NeurOST SSH-SST and DUACS. (iv) Time-series of coarse- and fine-scale KE (above and below coarse-graining scale of 125km respectively) from both NeurOST SSH-SST and DUACS. (v) Change in $KE_<$ (coarse-scale KE) from its wintertime minimum to its summertime maximum compared to the diagnosed contribution from the KE cascade ($-\int \Pi dt$), and the spatial transport of coarse-scale KE ($-\int \nabla \cdot Jdt$) for both NeurOST SSH-SST and DUACS. (b)(i-v) Same as (a)(i-v) but for the Subtropical South Pacific (194-206E, 19-31S). (c)(i-v) Same as (a)(i-v) but for the Kuroshio (153-167E, 29-41N). (d)(i-v) Same as (a)(i-v) but for the North Atlantic (322-338E, 39-51N) and with the dividing coarse-graining scale between fine- and coarse-scale KE reduced to 80km.

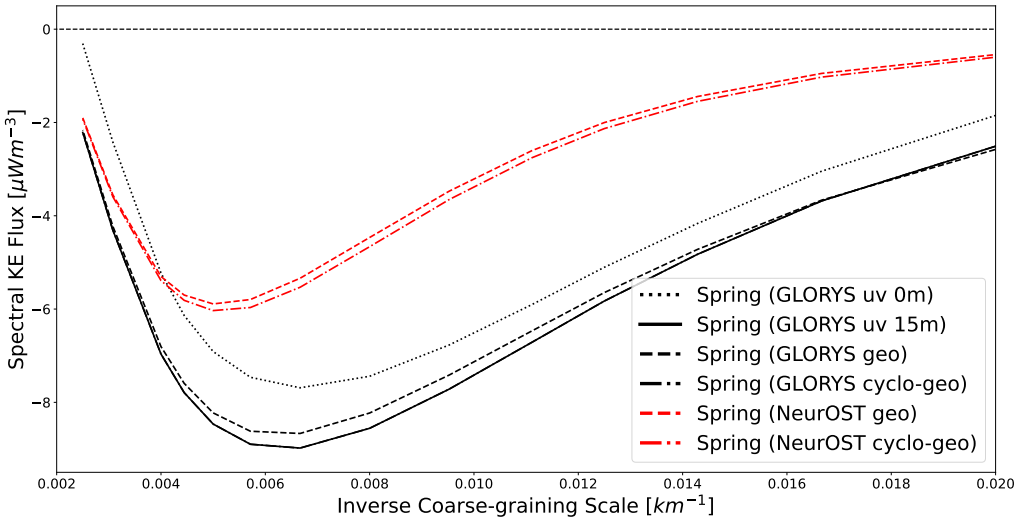


Figure S7: Springtime spectral KE flux estimated from GLORYS and the NeurOST reconstruction of GLORYS from synthetic observations (OSSE) in the Subtropical North Pacific. Results for GLORYS are presented using the total surface currents at 0m and 15m depths ('uv'), using surface geostrophic currents ('geo') calculated from SSH, and using the cyclo-geostrophic correction of Penven et al. (2014) ('cyclo-geo'). Results for NeurOST are presented for both geostrophic and cyclo-geostrophic currents.

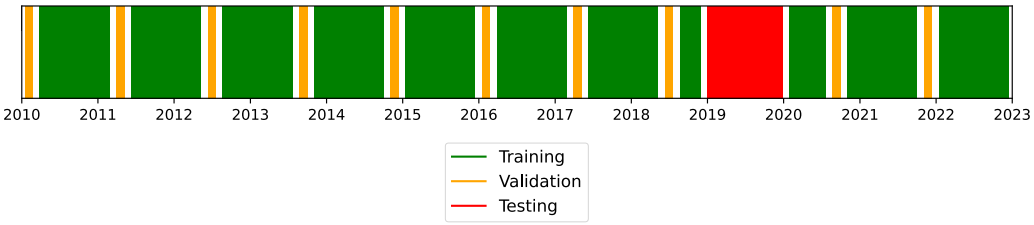


Figure S8: Partitioning of dates between training, cross-validation, and testing when training neural network for SSH mapping.

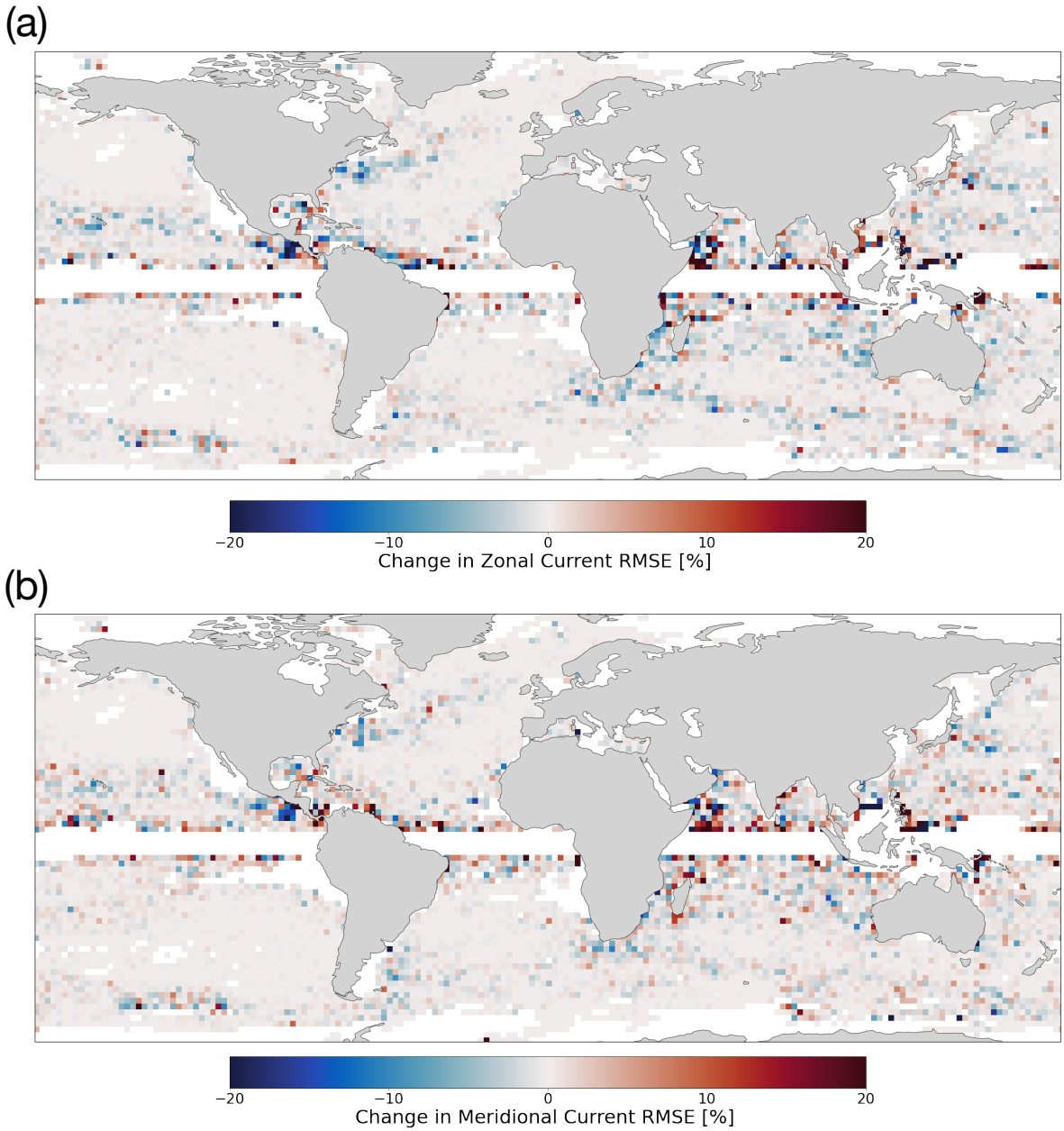


Figure S9: (a) Change in RMSE of zonal current evaluated using drifters when the cyclo-geostrophic correction of Penven et al. (2014) is applied to geostrophic currents from NeurOST SSH-SST. (b) Same as (a) but for meridional currents.

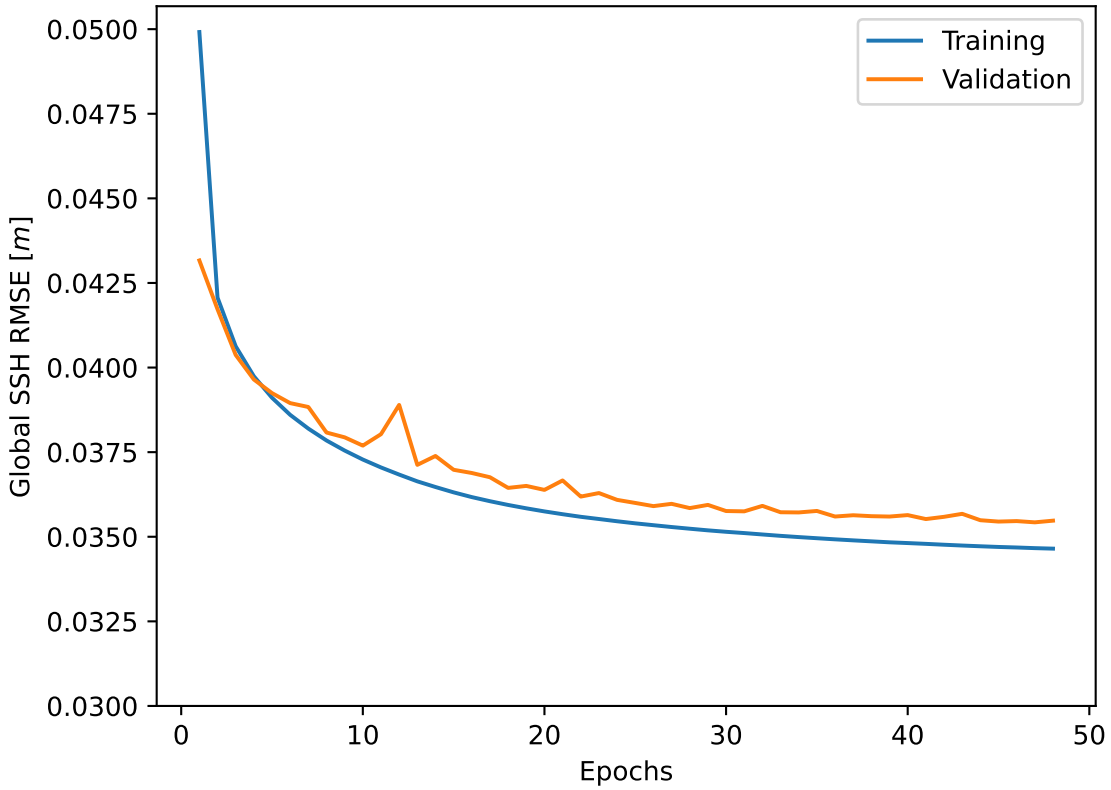


Figure S10: Learning curves for training of global NeurOST (SSH-SST) network showing globally averaged SSH RMSE on both the training and cross-validation datasets.

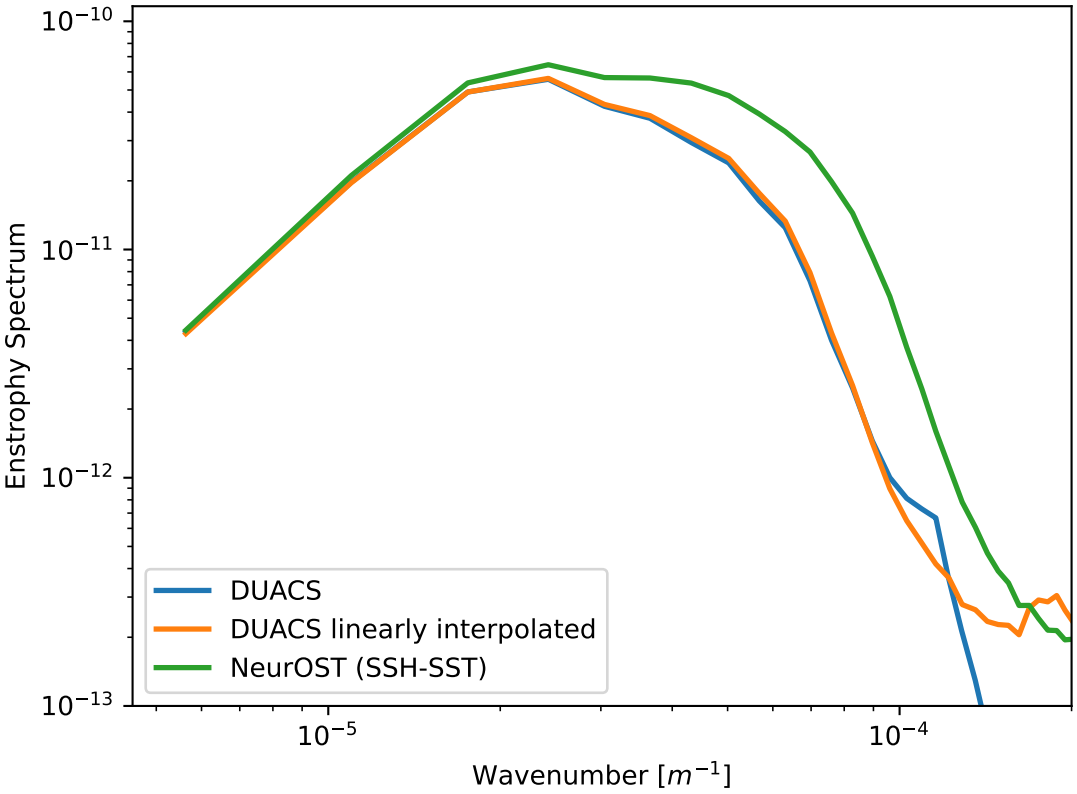


Figure S11: Enstrophy spectra in Subtropical North Pacific for DUACS, NeurOST, and DUACS but with velocities first linearly interpolated to the NeurOST grid spacing before estimating derivatives.